



The evaporite-coal transition: Chemical, mineralogical and organic composition of the Late Triassic Abu Ruweis Formation, NW Jordan—Reference type of the “Arabian Keuper”

H.G. Dill ^{a,*}, A. Bechtel ^b, Z. Berner ^c, R. Botz ^d, J. Kus ^a, C. Heunisch ^e, A.M.B. Abu Hamad ^f

^a Federal Institute for Geosciences and Natural Resources, P.O. Box 510163, D-30631 Hannover, Germany

^b Department of Applied Geosciences and Geophysics, University of Leoben, Peter Turner Strasse 5, A-8700 Leoben, Austria

^c Karlsruhe Institute of Technology, Institute for Mineralogy and Geochemistry, Adenauer Ring 20b, D-76131 Karlsruhe, Germany

^d University of Kiel, Geological-Paleontological Department, Olshausenstraße 40-60, D-24118 Kiel, Germany

^e Geological Survey of Lower Saxony, P.O. Box 510163, D-30631 Hannover, Germany

^f Department of Environmental and Applied Geology, University of Jordan, Amman 11942, Jordan

ARTICLE INFO

Article history:

Received 24 September 2010

Received in revised form 15 December 2011

Accepted 16 December 2011

Available online 11 January 2012

Editor: U. Brand

Keywords:

Chemofacies

Evaporites

Coal

Late Triassic

Keuper Facies

NW Jordan

ABSTRACT

The Abu Ruweis Formation, NW Jordan, was studied with regard to its chemical (major, minor elements, REE, S-, O-, C isotopes, organic chemistry), mineralogical compositions (rock-forming minerals), coal petrography (maceral analyses) and palynology (age determination and palaeosystem) for the evaporite-coal facies transition which is very rarely found. The palynomorphs point to a Late Triassic/Carnian age of formation. Strong evaporation in the series is demonstrated by the presence of dolomite, gypsum and celestite. Mg, Ca, F, Cl, S, Sr and Ba reflect the variation of evaporation during basin subsidence. A detrital influx is characterized by the abundance of Si, Ti, Al, Fe, Mn Ce, Co, Cr, V, Y and the (Zr + Rb)/Sr ratio. Salinity variation may be characterized by the fractionation of LREE (La) and HREE (Lu). The element triplet Zn, Cu and Pb offers a clue to the redox regime and supports the idea of mineralogical-based proximity indicators: Zn ($Eh \ll 0$) \Rightarrow Cu ($Eh \leq 0$) \Rightarrow Pb ($Eh \leq 0$). Oxygen isotope composition ($\delta^{18}\text{O}$ – 8.3 to – 0.9‰) of the carbonate fraction resulted in uniform isotope formation temperatures near 50 °C. Temperature data obtained during coal petrography yielded maximum paleotemperatures of 100 °C for the black shale and about 70 °C for the remaining coal samples that are likely to reflect hot brine activity in some parts of the basin. The carbon isotopic composition ($\delta^{13}\text{C}$ – 12.4 to – 3.9‰) of the carbonate fractions indicates a biogenic ^{12}C -enriched CO_2 source, which probably was admixed to marine pore water bicarbonate (with $\delta^{13}\text{C}$ near 0‰) during early diagenesis. The S isotope composition (sulfide fraction – 28.9 to – 24.0‰) is typical of sulfides formed in the course of bacterial reduction with some sulfate (sulfate fraction + 7.5 to + 11.6‰) resulted from later re-oxidation of the sulfides. Phosphate distribution is a measure for the aridity while high-sulfur contents in the coal-bearing sediments point to brackish or alkaline waters. The results of the organic chemistry are interpreted in terms of a bloom of algae which were preserved during dysaerobic conditions in the course of early diagenesis. Sesqui- and diterpenoids are most probably derived from precursor molecules abundant in leaf resins of conifers. Phenanthrene and its methylated analogues derived from combustion products of fossil fuels generated by wild fires. Among the maceral types, textinites A and B represent xylem features of tree trunks and the crassi-cutinite upper leaf cuticles. The data allow for a definition of a special geological setting called the “Arabian Keuper Facies”. This facies type is characterized by an evaporite-coal transition which translates into a geodynamic setting positioned between the fully marine “Alpine Triassic Facies” of the Tethyan Ocean where submarine brines were responsible for the Alpine-type MVT Pb-Zn deposits and the epicontinental “Germanic Keuper Facies” that lacks both hydrothermal activity and major marine incursions.

© 2012 Elsevier B.V. All rights reserved.

1. Introduction

The majority of coal seams are interbedded with siliciclastic sediments in continental and near-shore marine depositional environments (Teichmüller, 1989; Diessel, 1992; Galloway and Hobday, 1996; Makaske, 2001; Thomas, 2002; Moore and Shearer, 2003;

* Corresponding author.

E-mail address: dill@bgr.de (H.G. Dill).

URL: <http://www.hgeodill.de> (H.G. Dill).

Kalkreuth, 2004). However, there are far fewer instances of coal-forming sedimentary environments in calcareous platform sediments (Hamrla, 1959; Shao et al., 2003; Liu et al., 2004; Dill et al., 2007). Evaporites normally do not host coal seams or carbonaceous sedimentary rocks (Warren, 2006). Therefore, little is known about the evaporite-coal transition and its response to chemical facies changes (Waldrön and Rygel, 2005). The upper Triassic Abu Ruweis Formation is well exposed by open cut operations for gypsum in NW Jordan, which facilitate study of the gradual transition from the whitish evaporite cyclothsems into the dark coal beds overlain by red bed sediments (Fig. 1). This reference-type section was subjected to an in-depth study involving the chemical composition (major, minor elements, REE, organic chemistry, S-, O-, C isotopes), lithology, coal petrography and palynology (age of formation). The principal goal of the present study is to constrain the physico-chemical regime of this transitional organic-inorganic sedimentary facies. As a reference for the “Arabian Keuper Facies”, as many chemical and mineralogical data as possible have been collected and interpreted so as to allow for an adequate correlation with similar peculiar lithologies elsewhere and for an assessments of their economic potential.

2. Geological setting

The Triassic strata wedge out from N to S in the study area. A general stratigraphic section shows the upper Triassic beds of the Abu Ruweis Fm. (= formation) to conformably overlie the limestones and marly claystones of the Umm Tina Fm. (Table 1). The older Umm Tina and Abu Ruweis Fm., in particular, formed under restricted conditions conducive to thick evaporite beds which together with the coal-bearing facies form the basis of this study. Evaporitic facies are exposed in the lower course of the River Zarqa and are overlain by brown calcareous sandstones of Jurassic age (Bender, 1974; Bandel

and Khoury, 1981; NCJSC, 2000). The entire sequence measures 42 m in thicknesses (Table 1).

3. Methodology

The evaporitic-coal-bearing series was logged in the gypsum quarries at different spacings. 50 samples were taken for different follow-up in-house chemical and mineralogical analyses (Appendix 1).

Laboratory-based investigations involved routine optical mineralogical examination supplemented by XRD and SEM-EDS. For X-ray diffraction, a Philips diffractometer PW 3710 (40 kV, 30 mA) with CuK α radiation was used. The scanning electron microscope FEI QUANTA 600 FEG with an energy-dispersive system (SEM-EDS), was used to assist in mineral identification and for morphological studies.

The organic material (OM) was studied for its coal petrographic parameters and its palynological inventory at BGR and LIAG, Hannover. The dried samples were crushed, vacuum-embedded with epoxy resin and examined following the guidelines and the nomenclature of the ICCP system (ICCP, 1998, 2001). 50 textinite B/vitrodetrinitite particles were measured using a Leica DMRX microscope system for incident white and fluorescent light microscopy and digital images analyses. The total carbon (TOC) and total sulfur (TS) contents were determined on a Leco elemental analyzer at Leoben Technical University. The TOC was measured with the same instrument on samples pretreated with concentrated hydrochloric acid. For organic geochemical analyses, representative portions of selected samples were extracted for approximately 1 h using dichloromethane in a Dionex ASE 200 accelerated solvent extractor at 75 °C and 50 bar. After evaporation of the solvent to 0.5 ml total solution in a Zymark TurboVap 500 closed cell concentrator, asphaltenes were precipitated from a hexane-dichloromethane solution (80:1) and separated by centrifugation. The fractions of the hexane-soluble OM were separated into NSO compounds, saturated hydrocarbons, and aromatic hydrocarbons by medium-pressure liquid

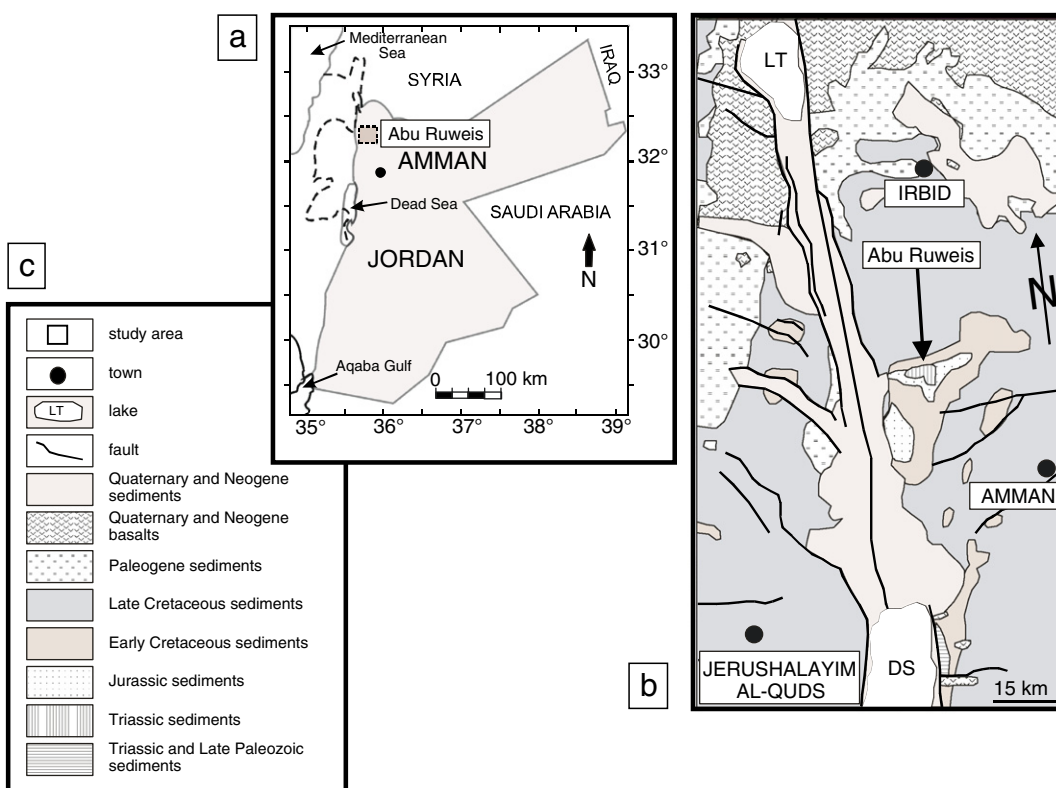


Fig. 1. Sketch maps to show the geological setting and topographic position of the study area of Abu Ruweis Formation, NW Jordan. a) Topographic position of the study area in the Hashemite Kingdom of Jordan. b) Geological setting of the study area based on the map “International Geological Map of Europe and the Mediterranean Regions 1:1 500 000, Map Sheet F 7 Amman. (Toloczyki et al., 1999). LT: Lake Tiberias (Sea of Galilee), DS: Dead Sea. c) Key to the geological map shown in panel b.

Table 1

Stratigraphic position of the Abu Ruweis Formation within the Mesozoic stratigraphy of Jordan (Bandel, 1981; Makhlof et al., 1990; Andrews et al., 1992; Khalil and Muneizel, 1992; Abu Hamad, 1994; Makhlof, 1998, 1999).

System	Series	Stage	Formation	Lithology	Thick. (m)
JURASSIC	Late	Tithonian	Mughanniyya	Dolomite, dolomitic sandstone, sandstone, limestone, marl, silty claystone and shale	110–120
		Kimmeridgian			
		Oxfordian			
	Middle	Callovian	Hamam	Claystone, sandstone, limestone and dolomite	60
		Bathonian	Ramla	Sandstone, clay and siltstone,	80
		Bajocian	Dhahab	Limestone, marl and silty dolomite	60
	Early	Aalenian	Silal	Conglomeratic sandstone, siltstone, silty claystone and dolomite	60
		Toarcian	Nimr	Limestone, dolomite clay, siltstone and sandstone	20
		Pliensbachian			
TRIASSIC	Late	Sinemurian	Hihi	Silty mudstone, limestone and sandstone	20
		Hettangian			
		Rhaetian			
	Middle	Norian			
		Carnian	Abu Ruweis	Gypsum, siltstone, claystone, sandy dolomite, marly claystone, marly limestone and dolomitic limestone	42
		Ladinian	Umm Tina	Limestone, marly claystone, dolomitic and limestone	62
	Early	Iraq Al-Amir	Iraq Al-Amir	Sandy limestone, sandstone, marl, siltstone, claystone, dolomitic limestone, marly limestone and dolomite	95
		Anisian	Mukheiris	Sandstone, marly claystone, siltstone, limestone, marlstone and claystone	76
		Scythian	Hisban	Limestone and dolomitic limestone	30
		Ain Musa	Ain Musa	Limestone, claystone, siltstone, dolomitic limestone, dolomite, sandstone and marly claystone	100
		Dardur	Dardur	Bituminous marlstone, silty shale, sandstone, sandy dolomite, dolomite, siltstone and claystone	59
		Ma'in	Ma'in	Sandstone, siltstone, clay, rare limestone and dolomitic limestone	47

chromatography using a Köhnen-Willsch MPLC instrument (Radke et al., 1980). The saturated and aromatic hydrocarbon fractions were analyzed on a gas chromatograph equipped with a 30-m DB-1 fused silica capillary column (i.d. 0.25 mm; 0.25-μm film thickness) and coupled to a Finnigan MAT GCQ ion trap mass spectrometer. The oven temperature was programmed from 70° to 300 °C at a rate of 4 °C min⁻¹ followed by an isothermal period of 15 min. Helium was used as carrier gas. The sample was injected splitless with the injector temperature at 275 °C. The mass spectrometer was operated in the EI (electron impact) mode over a scan range from *m/z* 50 to *m/z* 650 (0.7 s total scan time). Data were processed with a Finnigan data system. Identification of individual compounds was accomplished based on retention time in the total ion current (TIC) chromatogram and comparison of the mass spectra with published data. Relative percentages and absolute concentrations of different compound groups in the saturated and aromatic hydrocarbon fractions were calculated using peak areas from the gas chromatograms in relation to those of internal standards (deuterated *n*-tetracosane and 1,1'-binaphthyl, respectively).

Major and trace elements were analyzed by X-ray fluorescence spectrometry (XRF) at BGR in Hannover on powdered samples (PANalytical Axios and a PW2400 spectrometer). Samples were prepared by mixing with a flux material and melting into glass beads which were analyzed by wavelength dispersive XRF (WD-XRF). To determine the loss on ignition (LOI) 1000 mg of sample material was heated to 1030 °C for 10 min. After mixing the residue with 5.0 g lithium metaborate and 25 mg lithium bromide, it is fused at 1200 °C for 20 min. The REE were analyzed by inductively coupled plasma quadrupole mass spectrometry (ICP-QMS). An Agilent 7500ce, a MicroMist concentric nebulizer, a Peltier-cooled spray chamber, the Plasma Forward Power and the Shield Torch System were used. The PP screw caps were rinsed twice with demineralised water (SERALPUR-90, 18.2 MΩ). Different rock certified reference materials were used for quality control (ZGI standards: GM, BM, Japanese standards: JG-1, JB-1; Chinese standards: GSS 1–8, NCS ZC

73006). A number of quintuple determinations were also carried out with the sediment standard NCS ZC 73006.

In order to distinguish between the isotope composition of oxidized and reduced sulfur species a simple two stage separation procedure was adopted for most of the sediment samples at Karlsruhe University. By reaction of the powdered material with a mixture of HCl conc. and CrCl₂, in a first step sulfides (mostly as pyrite) were converted to H₂S and trapped as CdS ("sulfide fraction"). Subsequently, after evaporating the supernatant reagents to dryness, sulfates in the residue were reduced with Thode solution (mixture of HI, H₃PO₂ and HCl) and collected similarly as CdS ("sulfate fraction"). Sulfur in the hematite and goethite ore was extracted with Thode solution without any pre-treatment ("total sulfur"). The isotope composition of sulfur in CdS and in untreated gypsum samples was determined in continuous flow technique in a mass spectrometer (IsoPrime, GV) coupled online with an element analyzer (EuroVector), using the IAEA standards S1, S2 and S3 for calibration. Each reported value is the average of independent measurements on three sample aliquots, with a standard deviation <0.2%. Data are reported in ‰ deviation relative to the V-CDT reference material.

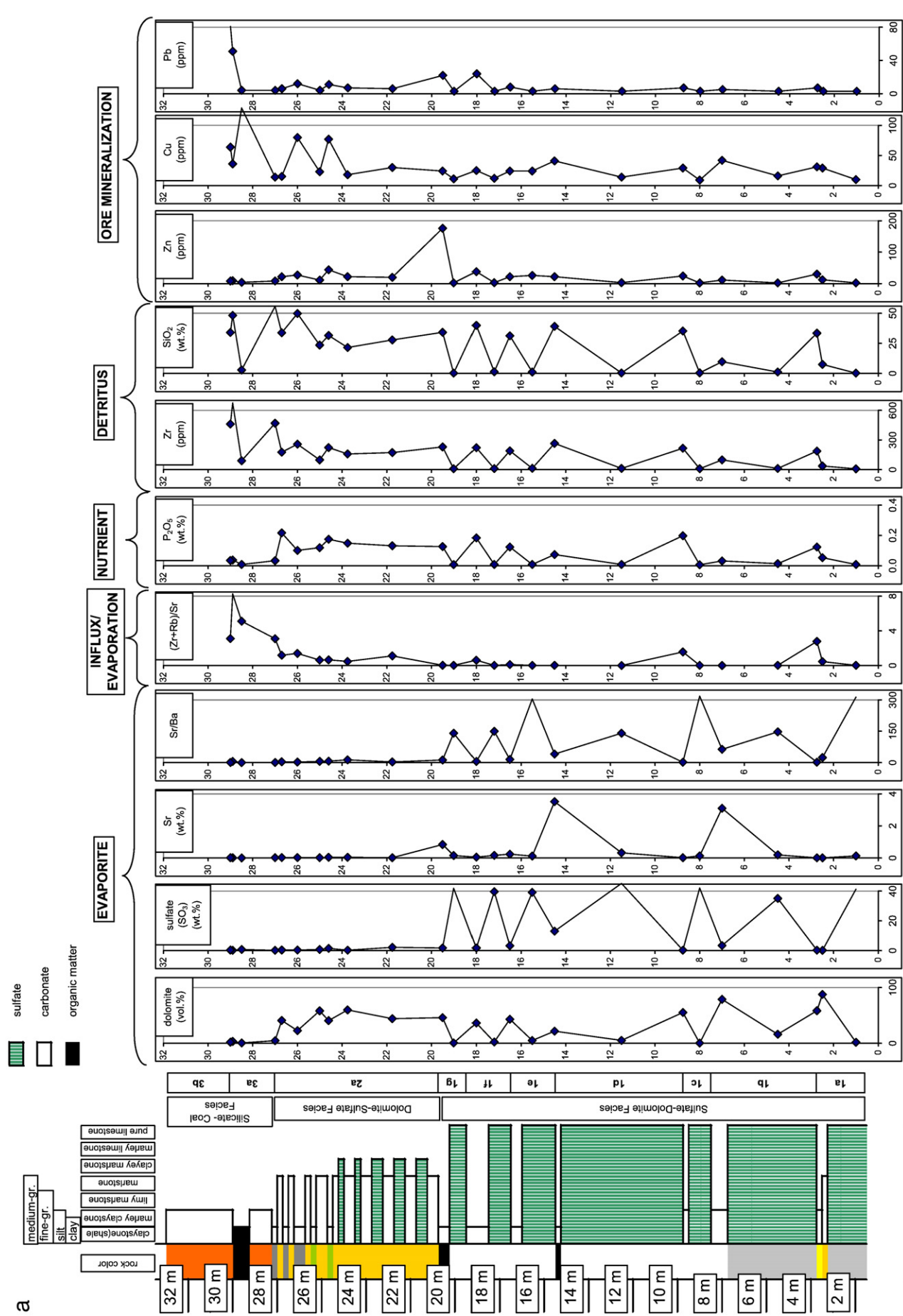
Carbonate isotope analyses were carried out according to McCrea (1950) at Kiel University. Bulk carbonate samples were reacted with 100% phosphoric acid and data reported in the δ-notation relative to the PDB standard (precision better than 0.1‰ for C and 0.15‰ for O).

4. Results

4.1. Lithology and mineralog

A cyclic variation may be recognized in the entire sedimentary record of the Abu Ruweis Fm. (Fig. 2a): 1st order classification scheme (Arabic numerals), 2nd order classification scheme (small caps). Seven subcycles may be identified, most of them of thinning-upward type.

Fig. 2. Lithochemistry including major and minor elements as a function of lithology and stratigraphy of the Abu Ruweis Formation and facies interpretation of the "Arabian Keuper Facies". a) Litholog and chemologs of major and minor showing the marker elements and ratios typical of sedimentary processes (evaporation, detrital influx, ore mineralization) and sedimentary components (evaporite, detritus, nutrient). For further chemologs see Fig. 9a (isotopes) and Fig. 10 (REE). 1. depth is given in meter 2. rock color 3. lithology is expressed as variable-width column (key on top) 4. Major and minor elements plus diagnostic element ratios. b) Synoptical overview of chemical, mineralogical and organic facies and the resultant analysis of the depositional environment of the Late Triassic Abu Ruweis Formation. The basin subsidence is given by the full line, the water/brine level by the dashed line (relative distance between bottom of the basin and water level) 1. chemofacies (inorganic) plus minerafacies 2. chemofacies (organic) plus coal facies 3. chemofacies (isotopic).



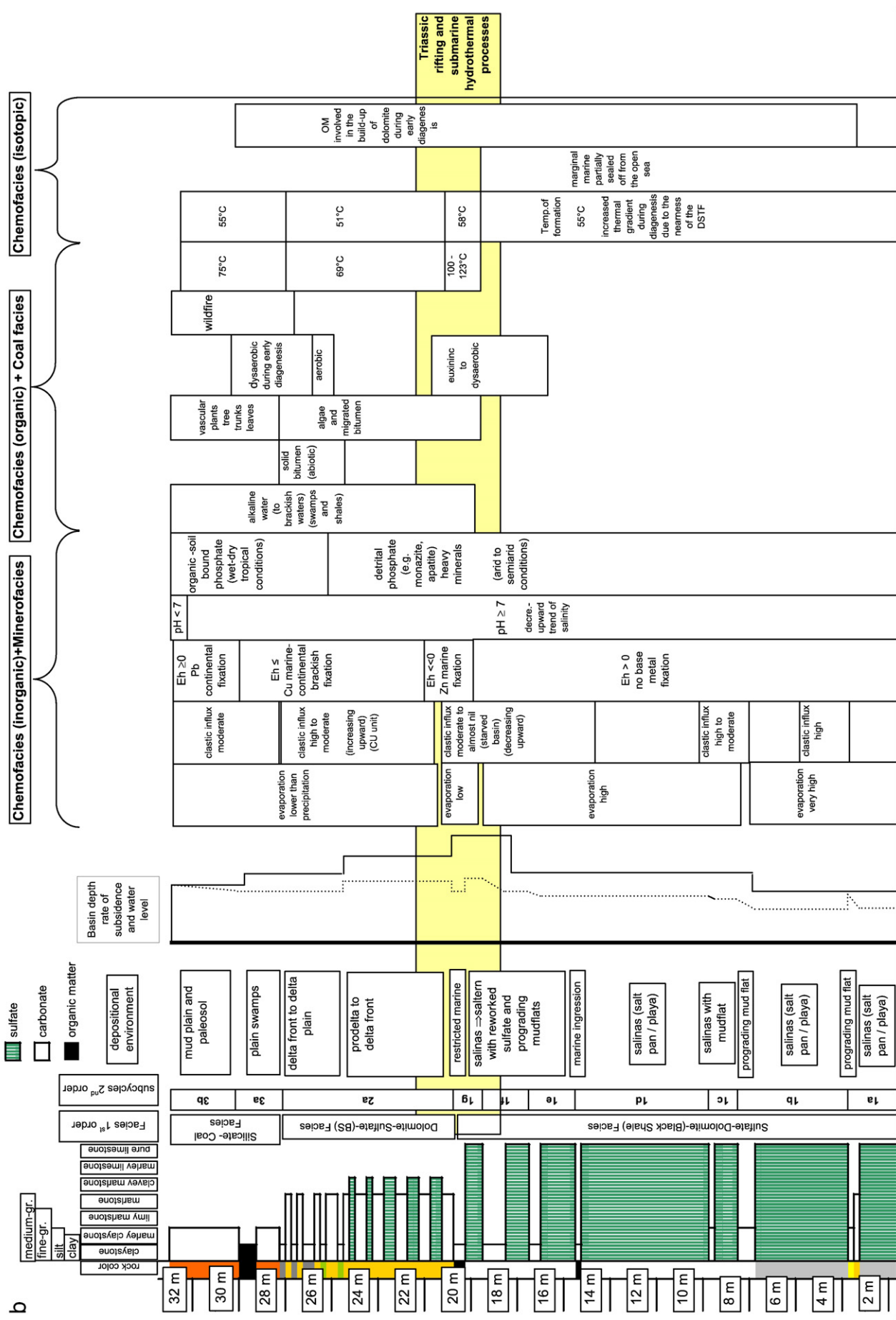


Fig. 2 (continued).



Fig. 3. Lithology of the sulfate- and dolomite facies of the upper Triassic Abu Ruweis Formation. a) Second-order cyclothem with gray massive to discontinuously laminated gypsum beds (gy) passing through yellowish clayey dolostones (do) into marly claystones (ms) on top (see also Fig. 2 cycle 1a). Lamination becomes more pronounced towards the dolomitic beds. b) Close-up view of the lower massive gypsum beds of Fig. 3a. c) Specimen of selenite from the gypsum layers within subcycles 1e through 1g. d) Convolute stratification within gypsum beds of subcycle 1e. e) Sedimentary unit (subcycle 2a) with horizontally well-bedded buff marlstone (ms) (minor contents of gypsum) alternating with gray green and dark gray claystones (cs). The topstratum is made up of hematized marly claystones (3a) (for cycle codes see also Fig. 2). Dotted line denotes the boundary between the two cycles.

4.1.1. Sulfate-dolomite facies

Thick gray massive to discontinuously laminated gypsum beds at the base pass up into yellow clayey dolostones (Fig. 3a). Eventually this lithological facies change terminates in calcareous beds traceable over a large distance. Each cycle fades out towards the top into marly claystones. In subcycles 1e through 1g fibrous selenite appears for the first time along bedding-plane parallel tension gashes. (Fig. 3c).

4.1.2. Dolomite-sulfate facies

In the dolomite-sulfate facies, gypsum rarely occurs as selenite in fractures of the horizontally well-bedded buff marlstone (Fig. 3e).

4.1.3. Silicate-coal facies

This unit which consists of a fully-developed fining-upward unit (FU) coded 3a is dominated by brown to red rock colors (Fig. 4).

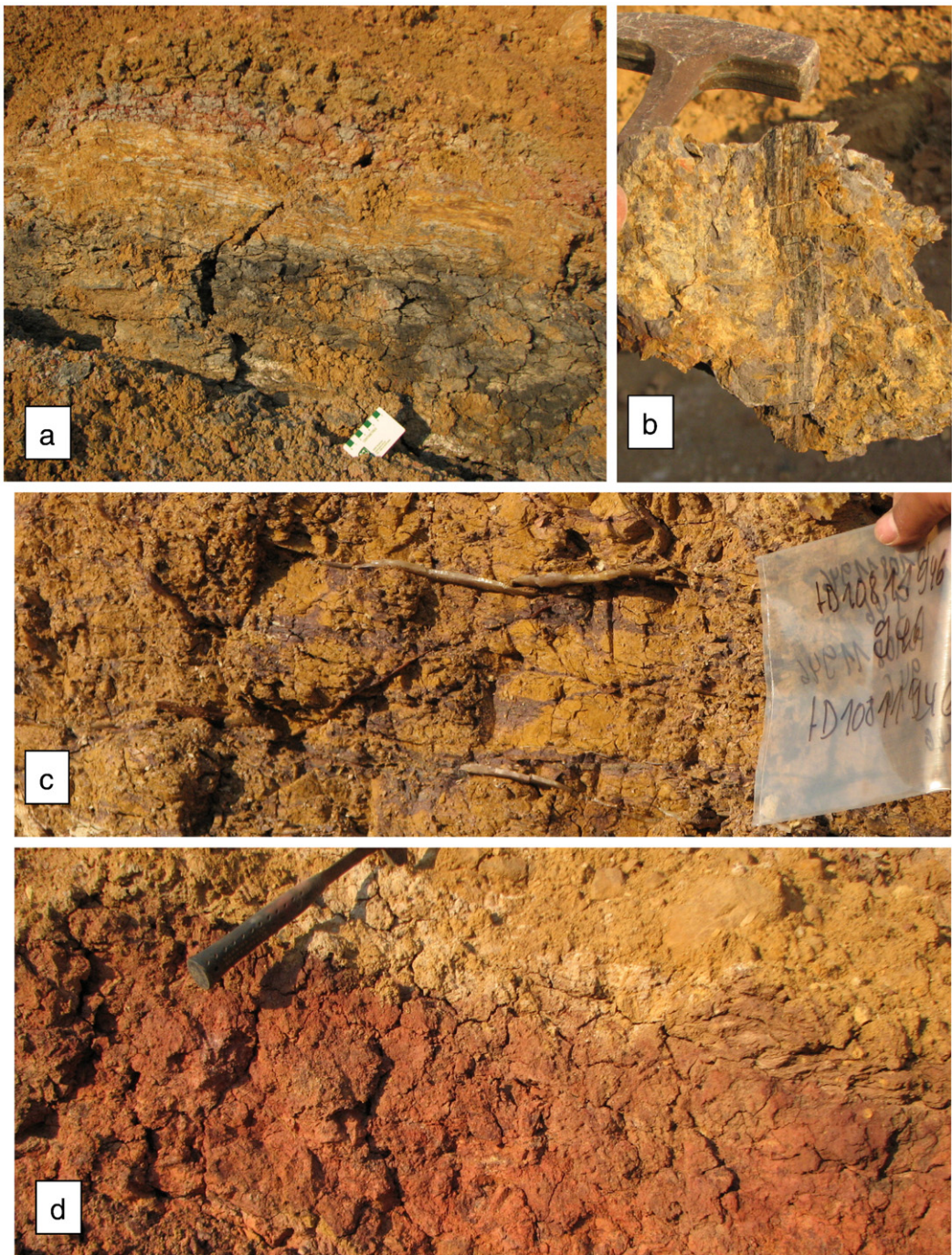


Fig. 4. Lithology of the silicate–coal facies of the upper Triassic Abu Ruweis Formation. For position of subcycles see Fig. 2. a) Coal seam of cycle 3a, overlain by a red paleosol. b) Remnants of a tree trunk which was accumulated as drift wood on top of the coal seam. c) Undulose fractures subparallel to the bedding planes filled with selenite (3b). d) Red to buff mottled pisolithic paleosol on top of the coal seam (subcycle 3b).

Only the organic-rich accumulations with scattered drift wood stand out by their gray color (Fig. 4a, b).

4.1.4. Mineralogy

The mineral assemblage of Abu Ruweis Fm. contains apart from ubiquitous gypsum, celestite and Ba-enriched celestite (Figs. 2, 5a). Relic anhydrite crystals are floating within subhedral crystals of gypsum (Fig. 5a). There is a gradual change from gypsum peppered with fine-grained dolomite aggregates through irregularly shaped nests of dolomite (Fig. 5b) into massive equigranular fine-grained dolomitic grainstone/marlstone (Fig. 5c). The fine-grained sediment shows

laminae rich in quartz and smectite–illite mixed layers which are the prevailing phyllosilicates (Fig. 5d). Pyrite is present in different quantities in the carbonate samples.

4.2. Coal petrography

The sediments contain terrestrial types III and II, and to a minor extent marine type-I kerogen. The detrital terrestrial origin of the dispersed OM is reflected by macerals of the huminite group and to a lesser extent by liptinite macerals (Table 2—10811947, 10811948, 10811950). The occurrence of marine dispersed OM is represented

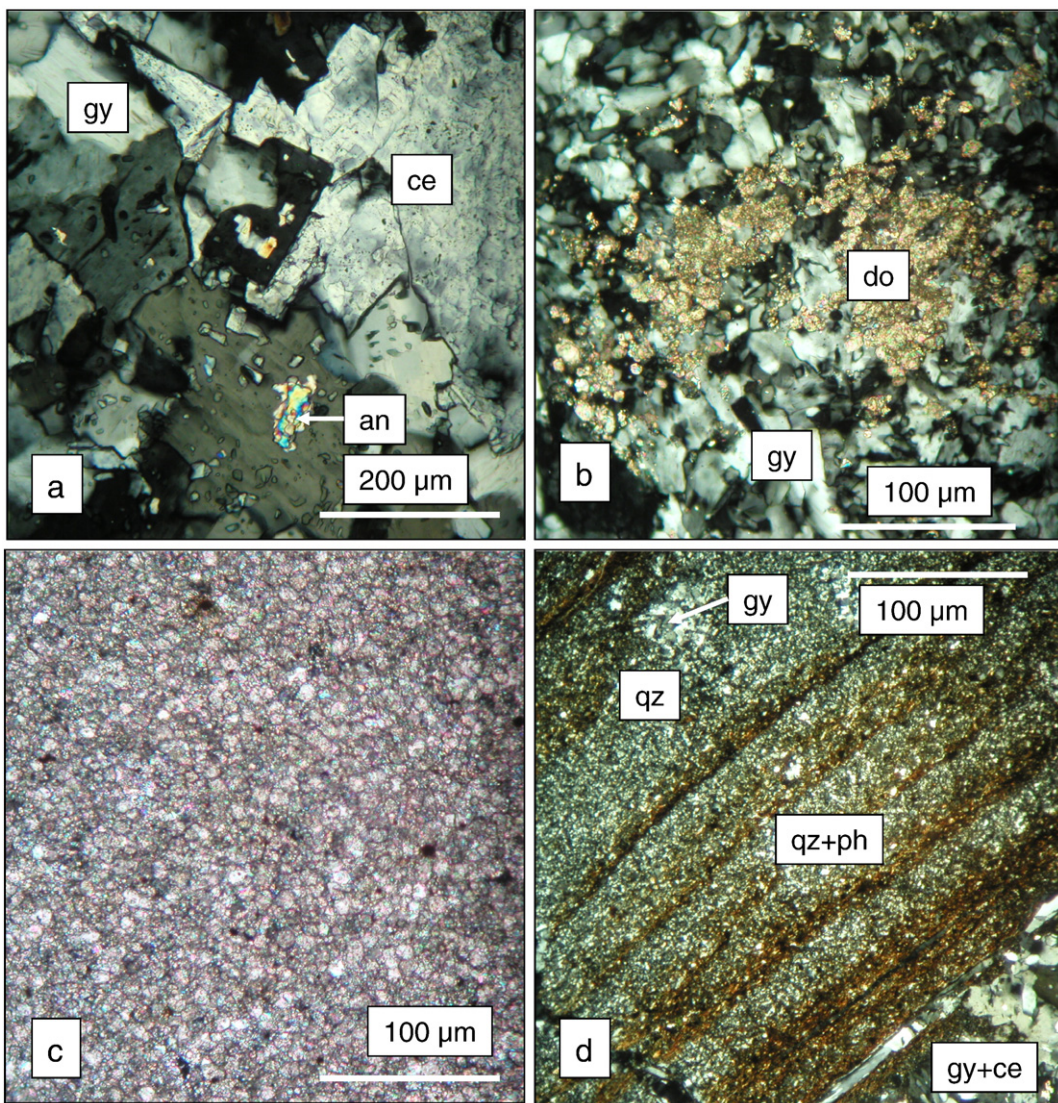


Fig. 5. Mineral assemblage of the evaporite facies in thin sections (grossed polars). a) Relic anhydrite (an) floating within subhedral crystals of gypsum (gy). They are replaced by celestite (ce) ($\text{Sr/Ba} = 63.4$) in the topmost part of subcycle 1b (see Fig. 2). b) Irregularly shaped nests of dolomite signal the passage into the overlying marly claystones and dolostones (subcycle 1c). c) Equigranular fine-grained dolomitic grainstone/marlstone (topstratum of subcycle 1a). d) Organic-rich calcareous clay shale atop of subcycle 1d. At the passage from the sulfate to the carbonate facies gypsum and celestite evolved (gy + ce). The fine-grained sediment shows conspicuous lamination and graded bedding with laminae rich in quartz and smectite-illite mixed layers (qz + ph). The topmost part contains some quartz (qz) and a nest of gypsum (gy).

by lamalginite (Fig. 6b). In coals, the terrestrial OM is dominated by textinite A and B and by ulminite macerals in the low rank coal of sub-bituminous stage (Fig. 6c–d) and vitrodetrinitite in the black shale (Fig. 6a). Within the liptinite macerals, cutinites represent a thick wall variety, i.e., crassi-cutinite (Fig. 6e–f). The folded leaf

cutinite displays in horizontal sections arrangements of well preserved intensively yellow to pale brown fluorescing epidermal cells with distinct anticlinal walls (Fig. 6g–h). Among the intensively yellow to pale brown fluorescing epidermal cells well preserved stomata and its surrounding guard cells are observed in both, horizontal and

Table 2

Coal petrographic analyses of samples from the “dolomite–sulfate”- and “silicate–coal” facies.

Sample number	Random vitrinite reflectance % R _r	Number of measurements N	Standard deviation S	Qualifier Q	Indicators of depositional environment	Temperature (maximum) (°C)
10810858 (1)	0.65	19	0.05	3	Black shale, DOM of predominately terrestrial origin with presence of aquatic lamalginite	100.7
10810858 (2)	0.86	56	0.07	5	Black shale, DOM of predominately terrestrial origin with presence of aquatic lamalginite	123.3
10811947	0.44	50	0.04	5	Humic coal, terrestrial origin	69.3
10811948	0.47	15	0.06	3	Coaly bands, streaks interspersed with carbonates and abundant pyrite; input of terrigenous organic matter	74.6
10811950	0.47	41	0.06	4	Coaly bands, streaks interspersed with carbonates extremely interspersed with massive pyrite or their aggregates; terrigenous organic matter	74.6

cross-sections. Directly below the epidermal cells with stomatal apparatus and bases for hairs or trichomes a weakly pale yellow to olive green fluorescing layer is observed. It is of <20 µm thickness

and in part interspersed with numerous non-fluorescent internal reflections (Fig. 6h). Also columnar cells of palisade parenchyma and green fluorescent fluorinites are also found (Fig. 6g).

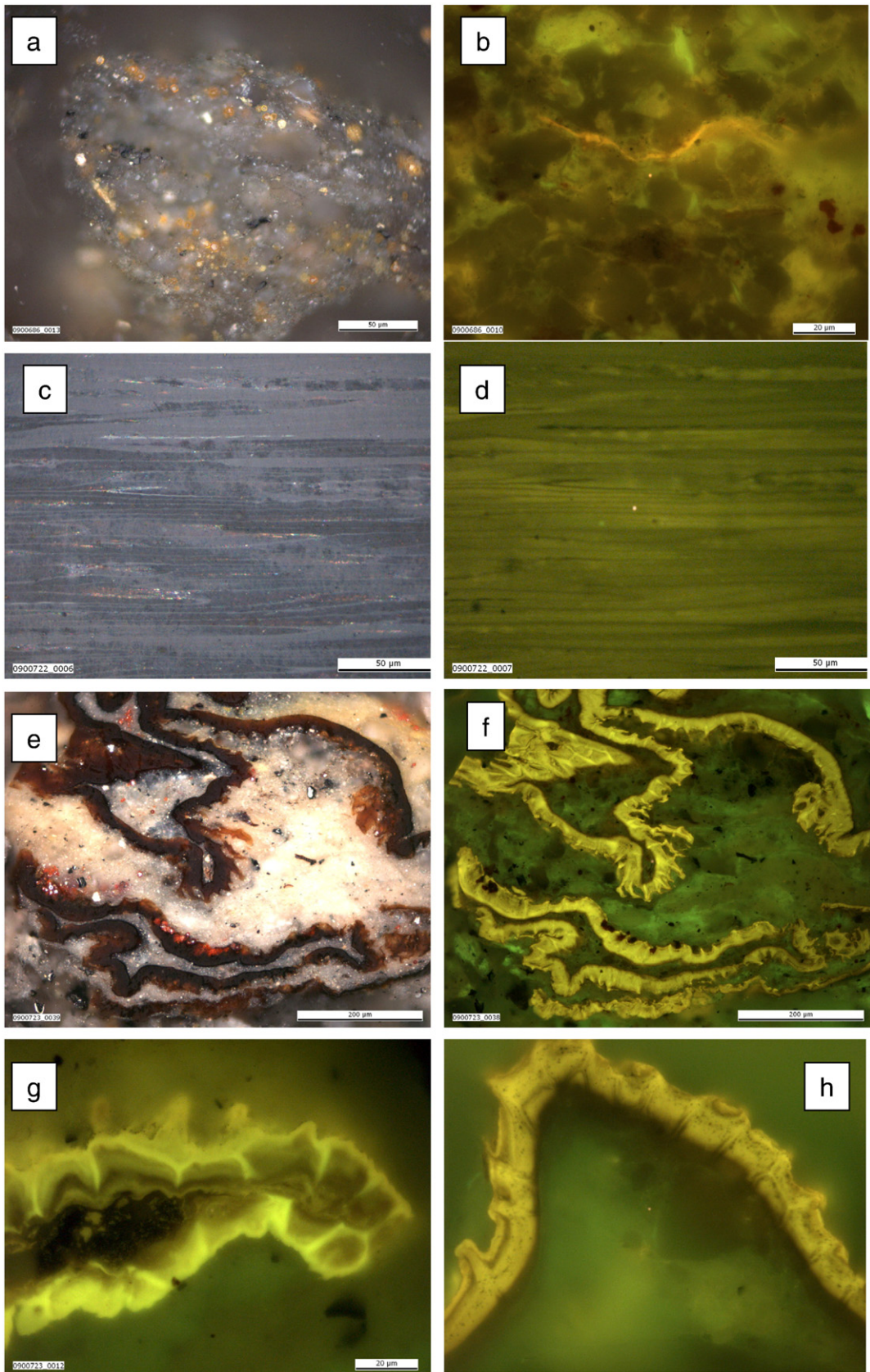


Table 3

Correlation of elements of the evaporite-coal transition. Correlation coefficients >+0.5 are marked in red.

	Depth	Dolo	SiO ₂	TiO ₂	Al ₂ O ₃	Fe ₂ O ₃	MgO	CaO	Na ₂ O	K ₂ O	P ₂ O ₅	SO ₃	Cl	F	As	Ba	Ce	Co	Cr	Cu	Ni	Pb	Sr	Th	U	V	Y	Zn	Zr
Depth	1.00																												
Dolo	-0.27	1.00																											
SiO₂	0.52	0.16	1.00																										
TiO₂	0.64	-0.09	0.88	1.00																									
Al₂O₃	0.64	-0.02	0.89	0.97	1.00																								
Fe₂O₃	0.68	-0.23	0.60	0.74	0.69	1.00																							
MgO	-0.27	1.00	0.16	-0.09	-0.02	-0.23	1.00																						
CaO	-0.65	-0.04	-0.84	-0.82	-0.82	-0.88	-0.04	1.00																					
Na₂O	0.33	0.16	0.68	0.63	0.57	0.46	0.16	-0.63	1.00																				
K₂O	0.28	0.37	0.76	0.43	0.53	0.14	0.37	-0.54	0.55	1.00																			
P₂O₅	0.16	0.60	0.54	0.23	0.32	0.04	0.60	-0.36	0.42	0.82	1.00																		
SO₃	-0.46	-0.57	-0.75	-0.63	-0.66	-0.61	-0.57	0.83	-0.57	-0.61	-0.61	1.00																	
Cl	-0.77	0.00	-0.34	-0.44	-0.48	-0.59	0.00	0.53	-0.20	-0.18	-0.23	0.51	1.00																
F	-0.54	0.54	0.03	-0.10	-0.08	-0.12	0.54	-0.02	0.23	0.08	0.20	-0.22	0.21	1.00															
As	0.35	-0.18	0.23	0.27	0.18	0.68	-0.18	-0.60	0.34	0.05	0.05	-0.38	-0.41	-0.01	1.00														
Ba	-0.01	0.17	0.29	0.07	0.02	0.07	0.17	-0.23	0.12	0.31	0.07	-0.23	0.27	-0.01	0.20	1.00													
Ce	0.62	0.04	0.79	0.84	0.81	0.62	0.04	-0.69	0.67	0.51	0.50	-0.62	-0.55	-0.10	0.29	-0.14	1.00												
Co	0.53	-0.16	0.31	0.31	0.37	0.57	-0.16	-0.63	0.29	0.31	0.05	-0.45	-0.48	-0.15	0.45	0.00	0.22	1.00											
Cr	0.64	-0.12	0.84	0.99	0.96	0.75	-0.12	-0.79	0.58	0.37	0.19	-0.59	-0.48	-0.10	0.26	-0.04	0.85	0.30	1.00										
Cu	0.38	-0.04	0.15	0.14	0.14	0.49	-0.04	-0.54	0.26	0.14	0.03	-0.43	-0.31	-0.02	0.54	0.13	0.10	0.76	0.13	1.00									
Ni	0.60	-0.12	0.39	0.44	0.46	0.80	-0.12	-0.77	0.36	0.24	0.12	-0.59	-0.60	-0.10	0.72	0.05	0.35	0.87	0.42	0.72	1.00								
Pb	0.41	-0.20	0.41	0.58	0.42	0.62	-0.20	-0.50	0.63	0.05	0.01	-0.32	-0.31	-0.14	0.62	0.09	0.65	0.23	0.55	0.24	0.43	1.00							
Sr	-0.24	0.21	0.00	-0.15	-0.20	-0.20	0.21	0.06	-0.02	0.07	-0.11	-0.01	0.53	0.11	-0.10	0.83	-0.34	-0.19	-0.23	0.05	-0.23	-0.10	1.00						
Th	0.40	-0.02	0.66	0.70	0.62	0.43	-0.02	-0.53	0.47	0.32	0.04	-0.41	-0.03	-0.13	0.10	0.52	0.50	0.06	0.65	0.09	0.10	0.45	0.50	1.00					
U	0.38	-0.18	0.32	0.53	0.35	0.59	-0.18	-0.45	0.59	-0.07	-0.06	-0.30	-0.29	-0.13	0.60	0.02	0.62	0.14	0.53	0.31	0.34	0.94	-0.10	0.46	1.00				
V	0.67	-0.12	0.76	0.85	0.80	0.87	-0.12	-0.88	0.56	0.33	0.20	-0.67	-0.56	-0.07	0.53	0.01	0.80	0.46	0.88	0.45	0.60	0.57	-0.20	0.57	0.62	1.00			
Y	0.66	0.04	0.87	0.95	0.92	0.76	0.04	-0.83	0.67	0.47	0.38	-0.73	-0.57	-0.06	0.36	0.00	0.91	0.29	0.95	0.16	0.47	0.58	-0.25	0.61	0.57	0.89	1.00		
Zn	0.09	0.28	0.30	0.13	0.12	-0.02	0.28	-0.18	0.09	0.45	0.40	-0.29	-0.15	0.00	0.22	0.51	0.11	0.02	0.05	0.01	0.09	0.12	0.10	0.09	0.01	0.04	0.17	1.00	
Zr	0.61	-0.11	0.84	0.97	0.89	0.79	-0.11	-0.83	0.65	0.35	0.15	-0.62	-0.40	-0.09	0.41	0.19	0.80	0.27	0.95	0.19	0.45	0.66	-0.03	0.76	0.65	0.89	0.94	0.13	1.00

Vitrinite reflectance shows a narrow coalification range corresponding to low rank A coal of a sub-bituminous B stage (Table 2). Similarly, a narrow range of thermal maturity in sedimentary rocks averaging to 0.46% R_r indicates an immature stage of oil and gas generation in the carbonate succession. The black shale samples represent, however, an exception to the overall thermal maturity pattern. They are characterized by elevated vitrinite reflectances with two clearly discernable populations at 0.65 and 0.82% R_r, respectively.

4.3. Palynology

Besides some OM which was investigated in detail in the previous chapter, the carbonaceous sediments of the silicate-coal facies are abundant in palynomorphs such as *Corollina meyeriana*, *Spirisporites spirabilis* and *Foveosporites* sp.

4.4. Major and minor element distributions

The chemical composition of the Abu Ruweis Fm. is given in Appendix 1 while the correlation of major and minor elements is illustrated in Table 3. Some selected elements plotted as a function of stratigraphy and the lithofacies (environment of deposition) form the basis for the chemical facies analysis *sensu* Adams and Weaver (1958), Bhatia and Cook (1986), Cox et al. (1995), Dean and Arthur (1998), Dypvik and Harris (2001). An increasing-upward trend has been reported for Si, Ti, Al, Fe and Mn (Appendix 1). This is also true for Ce, Co, Cr, V, Y and Zr among the minor elements. All of them have correlation coefficients greater than +0.5 as being correlated with depth (Table 3). Mg, Ca, F, Cl, S, Sr and Ba show an antithetic trend to depth (Table 3). A couple of elements do not show a stratigraphy- or facies-related trend. The maximum Zn content has

Fig. 6. Photomicrographs of coal, coaly and dispersed OM obtained during organic petrographic studies of the dolomite-sulfate- and silicate-coal facies of the Abu Ruweis Formation. a) Finely dispersed vitrodetrinitite particles and iron oxides/hydroxides in the black shale lithofacies in white light mode. b) Subdued pale orange fluorescent lamalginitite in blue light mode. c) Tangential section of fossil wood. Xylo-texinite B. Cells are in part filled with resinite in white light mode. d) Tangential section of fossil wood. Dark olive green fluorescent xylo-texinite B. Cells are in part filled with pale green fluorescent resinite in blue light mode. e) Crassi-cutinite in cross-section embedded in carbonates in white light mode. f) Pale to intensive yellow fluorescent crassi-cutinite in cross-section embedded in carbonates in blue light mode. g) Cross-section of leaf cuticle displaying crassi-cutinite with well preserved multilayered structure of epidermal cells dissected by distinct anticlinal walls with spongy mesophyll cells in blue light mode. h) Cross-section of crassi-cutinite with well preserved multilayered structure of epidermal cells characterized by spotted appearance.

Table 4a

Chemical composition of the organic material. Bulk organic geochemical parameters.

Sample	Lithology	TOC (wt.%)	TS (wt.%)	EOM (mg/g TOC)	Sat. HC (%)	Arom. HC (%)	NSO (%)	Asphalt. (%)
10811950 (1)	Coal	9.44	12.54	3.17	13	10	37	40
10811950 (2)	Coal	9.33	13.04	6.72	10	7	35	48
10811948 (1)	Coal	4.02	2.24	9.36	7	5	58	30
10811948 (2)	Coal	4.48	1.64	7.93	n.a.	n.a.	n.a.	n.a.
10811947 (1)	Coal	70.25	2.18	4.30	3	5	24	68
10811947 (3)	Coal	76.17	1.78	2.51	5	7	37	51
10810858 (BS)	Black Shale	3.57	1.09	11.43	26	6	44	23

TOC = Total organic carbon; TS = Total sulfur; EOM = Extractable organic matter; Sat. HC = Saturated hydrocarbons; Arom. HC = Aromatic hydrocarbons; NSO = NSO compounds; Asphalt. = Asphaltenes; n.a. = not analysed because of low amount of EOM.

Table 4b

Chemical composition of the organic material. Concentrations of individual compounds and compound groups as well as biomarker ratios.

Sample	n-Alkanes ($\mu\text{g/g}$ TOC)	CPI	Pr/Ph	Steranes ($\mu\text{g/g}$ TOC)	20S/(20S + 20R) C_{29} Steranes	Diasterenes ($\mu\text{g/g}$ TOC)	Hopanes ($\mu\text{g/g}$ TOC)	22S/(22S + 22R) C_{31} Hopanes	Sesqui- + Diterpenoids ($\mu\text{g/g}$ TOC)	PAH ($\mu\text{g/g}$ TOC)
10811950 (1)	40.98	1.55	1.21	1.63	0.27	n.d.	5.20	0.51	6.72	4.91
10811950 (2)	58.48	1.68	1.59	3.23	0.30	n.d.	10.26	0.48	7.69	4.28
10811948 (1)	108.14	1.61	1.47	4.11	0.24	2.02	10.86	0.45	15.57	16.91
10811947 (1)	5.76	1.38	2.53	1.27	0.26	4.45	1.88	0.49	15.14	4.91
10811947 (3)	2.58	1.45	2.33	1.77	0.28	2.57	1.52	0.47	9.52	5.00
10810858 (BS)	116.59	1.35	0.93	29.81	0.31	9.52	19.88	0.44	46.50	9.67

CPI = Carbon preference index; Pr = Pristane; Ph = Phytane; Homopreg. = Homopregnane; Tricycl. = Tricyclic; TOC = Total organic carbon; PAH = Polycyclic aromatic hydrocarbons (4–5 rings); n.d. = not detectable.

been reported from the boundary between the sulfate and dolomite facies (Fig. 2a). The remaining base metals Cu and Pb are enriched in the silicate-coal facies, yet not in those beds which gave such a

pronounced peak as reported for Zn. P_2O_5 mean values show no remarkable highs when plotted as a function of stratigraphy (Fig. 2a). The OM is concentrated in discrete individual seams of different

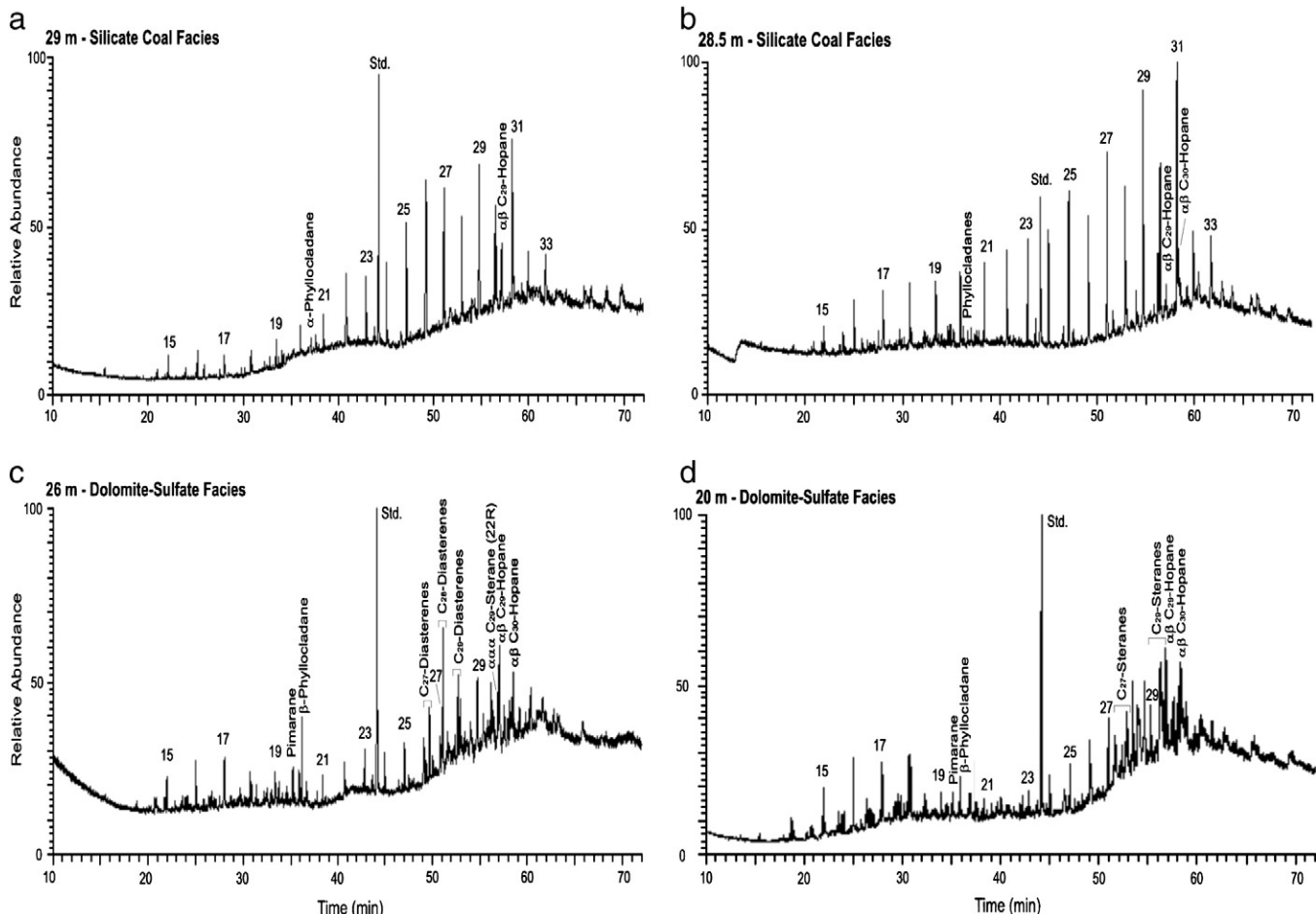


Fig. 7. Gas chromatograms (total ion current) of saturated hydrocarbon fractions of four samples from different stratigraphic levels and facies n-Alkanes are labelled according to carbon number. Std. = standard (deuterated n-tetracosane).

thickness. The TOC was therefore only analyzed in some of the samples and is given together with the chemical results obtained from organic chemistry (Table 4a).

4.5. Organic chemistry

The bulk chemical composition of the samples is characterized by high-sulfur (1.1 to 13.0 wt.%) and variable TOC contents (between 3.6 and 76.2 wt.%). Only the lignite-jet samples show TOC values expected for coals. Despite the high TOC contents, the normalized yields of the extractable OM (EOM) from the samples are low (between 3.2 and 11.4 mg/g TOC). The relative proportions of hydrocarbons of the EOM of most samples are low (between 8 and 23%), taking into account the elevated maturity (0.4–0.5% R_r) of the OM (Table 4a). Highest relative hydrocarbon contents are obtained from the coal-bearing samples and the black shale (32% of EOM). The extractable OM is mainly composed of NSO compounds (>25% of the EOM) and asphaltenes (between 23 and 68% of the EOM). The samples at 26 m are characterized by very high TOC contents, low extraction yields and high contents of resins. Molecular composition of hydrocarbons may be described as follows. The n-alkane patterns of most of the samples are dominated by long-chain n-alkanes (>n-C₂₇) with a marked odd over even predominance, as indicated by values of the Carbon Preference Index (CPI) between 1.4 and 1.7 (Table 4b; Figs. 7, 8). The CPI was calculated from the concentrations of individual n-alkanes using the formula according to Bray and Evans (1961). The samples taken at 28.5 m are characterized by nearly equal contents of short- (n-C_{15–19}), middle- (n-C_{21–25}) and long-chain n-alkanes and slightly lower CPI values (Table 4b; Fig. 7). The

black shale shows a bimodal n-alkane distribution with maximum intensities at n-C17 and n-C27, respectively.

In all samples, the 5 α ,14 α ,17 α (H) C₂₉ steranes, dominating over the 5 α ,14 β ,17 β (H) steranes, are found in concentrations sufficient for peak integration (Table 4b; Fig. 7). The C₂₇ and C₂₈ pseudohomologues are present in very low relative concentrations, with the exception of the black shale sample where higher concentrations of C₂₇ steranes were detected. The corresponding diasterenes could be detected in the sample at 28.5 m, 26 m and 20 m. In the sample at 26 m, the C₂₈ and C₂₉ diaster-13(17)-enes are present in higher concentrations than the steranes (Table 4b) and the C₂₈ diasterenes predominate over the C₂₉ diasterenes. C₂₉ and C₃₀ 4-methylsteranes are only present in low concentrations in the hydrocarbon fractions of lignite and blacks shale samples.

Hopanes are the predominant constituents of the non-aromatic cyclic triterpenoids in most samples. The samples show similar patterns, characterized by the occurrence of 17 α ,21 β (H)-type hopanes from C₂₇ to C₃₂, with C₂₈ hopanes absent. The 17 β ,21 α (H) hopanes from C₂₉ to C₃₁ are present in very low amounts. The predominant hopanoïd is either the $\alpha\beta$ -C₃₀ hopane or the $\alpha\beta$ -C₂₉ hopane (Fig. 7).

In all samples, the sesquiterpenoid cadalene predominate in the aromatic hydrocarbon fractions (Fig. 8). Further constituents of the aromatic sesquiterpenoids are calamenene (Simoneit and Mazurek, 1982) and a compound tentatively identified on the basis of its mass spectrum as des-methyl cadalene. The diterpanes in the saturated hydrocarbon fractions (Fig. 7) consist of the tetracyclic series (16 β (H)-phylocladane and 16 α (H)-phylocladane), as well as of pimarane and norpimarane (Philp, 1985). The aromatic diterpenoids present in the samples consist of compounds of the abietane-type

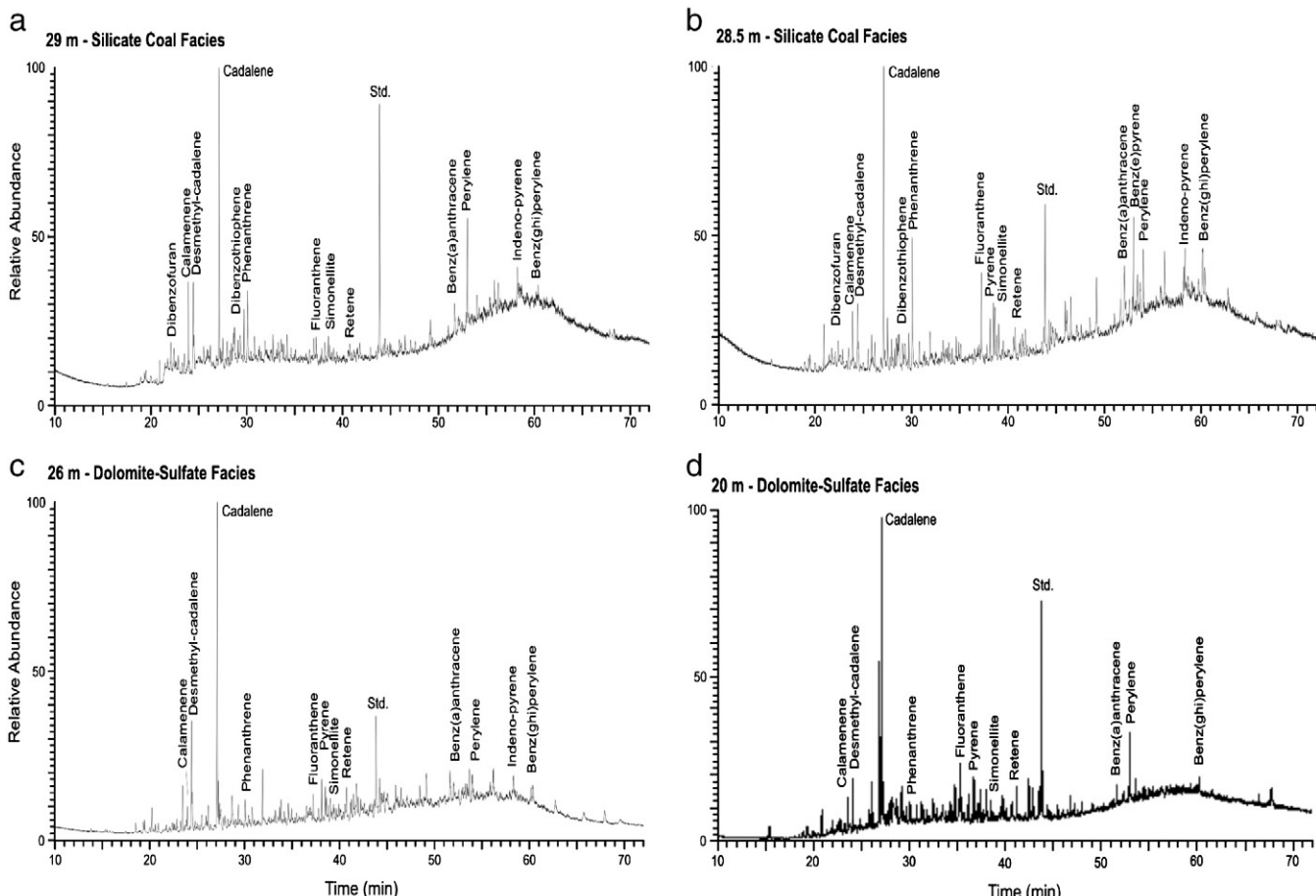
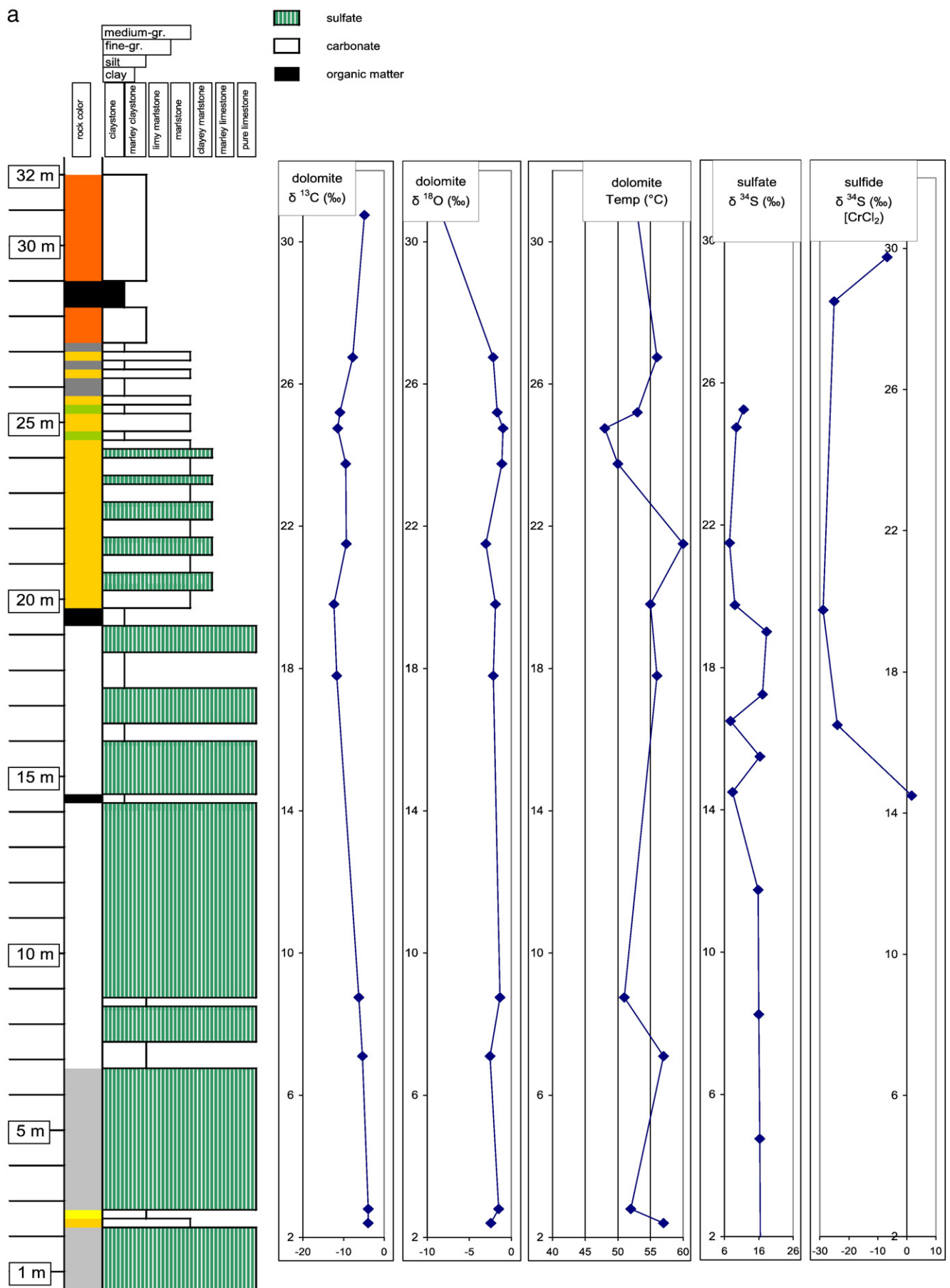


Fig. 8. Gas chromatograms (total ion current) of aromatic hydrocarbon fractions of four samples from different stratigraphic levels and facies Std. = standard (1,1'-binaphthyl).



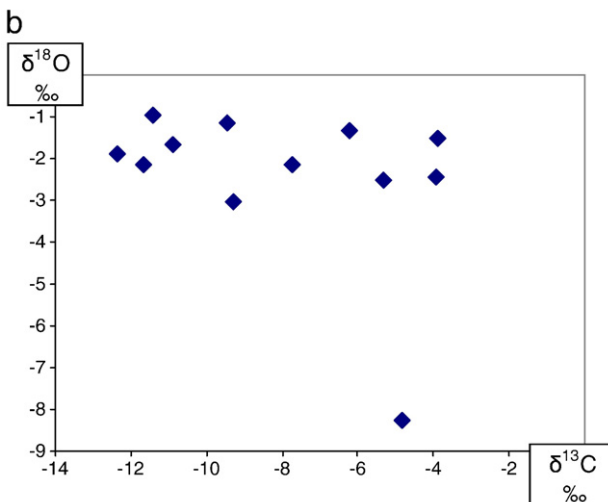


Fig. 9 (continued).

(e.g. simonellite, retene; Philp, 1985), with simonellite as the dominant compound in most samples (Fig. 8). The polycyclic aromatic hydrocarbon (PAH) phenanthrene is detected in all samples (Fig. 8).

4.6. Sulfur, carbon and oxygen isotopes

The isotope composition of gypsum sulfur in the lithological sequence in NW Jordan is in accord with that of evaporites of upper Triassic age found in other areas of the Alpino-Thetian realm (Longinelli and Flora, 2007). In the lower part of the sequence $\delta^{34}\text{S}$ values decrease upward from 16.5 to 15.8‰, and then reverse, increasing up-section to 18.3‰ (Fig. 9). Except for a selenite bearing black shale sample with $\delta^{34}\text{S} = 1.7\text{\textperthousand}$, the isotope composition of the sulfide fraction extracted from fine-grained sediments (shales and marls) shows consistently low values (−28.9 to −24.0‰). Compared to these, the sulfate fraction of the same samples is always less depleted in ^{34}S and varies in a relatively narrow range, between +7.5 and +11.6‰. While pyrite in the coal seam at 29 m has a similar isotopic composition to the sulfide fraction of the shales/marls (−25‰), the sulfide of the gagat yielded a considerably higher value (−6.8‰). The carbon and oxygen isotopes have been plotted for bulk carbonate fractions ($\delta^{13}\text{C}$ −12.4 to −3.9‰, $\delta^{18}\text{O}$ −8.3 to −0.9‰) alongside the litholog (Fig. 9a) and in a cross plot to illustrate a possible interrelationship between the sets of isotopes. There is no obvious correlation between the carbon and oxygen isotopes, however (Fig. 9b).

4.7. Rare earth elements (REE)

Results of REE analyses of the evaporite- and OM-bearing sediments presented in this paper were normalized to the post-Achaean Australian Shale (PAAS) after McLennan (1989). Based upon these diagrams the La/Lu ratios, the Eu and Ce anomalies were calculated. The cerium anomalies were calculated as Ce/Ce* ratios ($= \log \text{Ce}_{\text{norm}} / (\text{La}_{\text{norm}} + \text{Pr}_{\text{norm}})$) and the Eu anomalies as Eu/Eu* = Eu_{norm} (Sm_{norm}*Gd_{norm})^{0.5}. The Ce anomaly does not show any significant variation across the entire litholog (Fig. 10). The Eu anomalies although more variable in their distribution than the Ce anomalies do not reveal any trend or conspicuous relation to the lithology or stratigraphy, either. Only the La/Lu ratio shows a

clear decreasing-upward trend for the litholog under consideration in this evaporite-coal series (Fig. 10).

5. Discussion

5.1. Palynofacies—Age of deposition and biostratigraphic correlation

Based on the palynomorphs the age of the host series has to be assigned a Tuvalian age (uppermost Carnian/Late Triassic). Many of the species have also been recorded from the Germanic Facies in Poland and from Croatia (Orłowska-Zwolinska, 1983; Koch, 1998). *Corollina meyeriana* and *Spirisporites spirabilis* are typical of the upper "Gipskeuper" which extends from the Swiss Jura through Germany into Poland. Not of the same age but very much similar with regard to the depositional environment, the Purbeck–Wealden transitional facies at the passage from the Late Jurassic into the Early Cretaceous may be held equivalent to the facies under study in Jordan (Wilde and Schultka, 1996). Using the depositional associations for evaporite accumulations *sensu* Warren (2006), the paleogeographic scenario under study reflects an epeiric platform setting.

5.2. Inorganic chemofacies—Sedimentary processes

5.2.1. Evaporation

Dolomite, gypsum, represented in the chemofacies by the SO₃ content, and celestite represented by the Sr contents can both be used to describe the degree of evaporation in this epicontinental basin. A decrease in the rate of evaporation is also signaled by the Sr/Ba ratio which is governed by the salinity of the fluids. The ratio is rather high for cycle 1a, runs at an intermediate level until subcycle 1e and drops to a very low level in subcycles 1f and 1g. Higher up in the stratigraphic column the ratio of evaporation is smaller than 1, an idea corroborated by the onset of OM-bearing beds in the stratigraphic column. Along the Trucial Coast and in the Central European basin which was sealed off during the Middle Muschelkalk extensive evaporation caused strontianite, celestite and fluorite to form lenses and layers (Dill et al., 2008). Fluorine is an indicator for an intermediate level of evaporation and bound to the dolomite–sulfate facies as in many other epicontinental basins elsewhere. The BaSO₄ component within celestite becomes remobilized as a result of diagenetic and epigenetic processes under more reducing conditions. Mg, Ca, F, Cl, S, Sr and Ba are held to be the most suitable marker elements to characterize the rate of evaporation in this epicontinental basin (Table 3).

5.2.2. Detrital influx

A strikingly increasing-upward trend of Si, Ti, Al, Fe, Mn, Ce, Co, Cr, V, Y and Zr and a negative correlation (Table 3) refers to the detrital component of these heterolithic sediment. SiO₂ and Zr mirror the continental run-off and detrital influx into a basin dominated by chemical and biogenic sediments (Fig. 2a). The most suitable parameter to mark the detrital input into an evaporitic environment is the (Zr + Rb)/Sr ratio that combines the most diagnostic elements highlighting evaporation and detrital input (Dypvik and Harris, 2001). Zirconium stands for the arenaceous grain size, Rb for the argillaceous particle size and Sr is the protagonist on the evaporitic scene. Based upon that ratio, a continuous decrease in detrital material may be recognized from subcycle 1a through 1g. The dark shales of subcycle 1g, consequently, denote a starved basin, undernourished with regard to siliciclastic material. This bed marks a turn-around in the detrital influx, that steadily increased up to subcycle 3a and tips off again. The first low in detrital influx occurred under reducing

Fig. 9. Sulfur, oxygen and carbon isotopes as a function of lithology and stratigraphy of the Abu Ruweis Formation—see also Fig. 2. a) Sulfur, oxygen and carbon isotopes of bulk carbonate plotted as a function of stratigraphy and lithofacies (see also Fig. 2). The S isotope fraction labeled as "CrCl₂" refers to the sulfide fraction mostly as pyrite, the fraction labeled as "Thode" is equivalent to the sulfate fraction. b) $\delta^{13}\text{C}$ vs. $\delta^{18}\text{O}$ bulk carbonate.

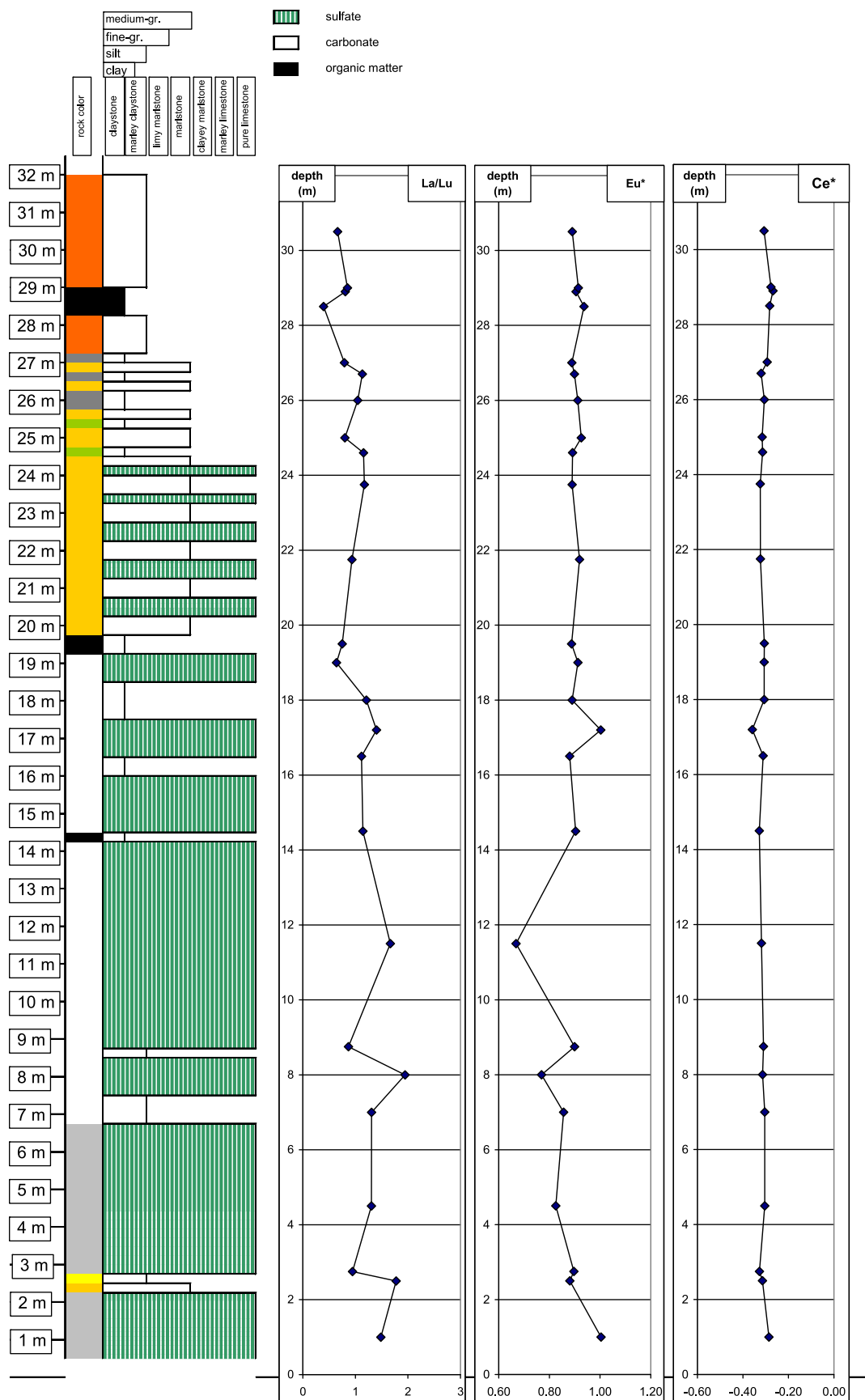


Fig. 10. REE variation as a function of lithology and stratigraphy of the Abu Ruweis Formation—see also Fig. 2. a) La/Lu fractionation (LREE/HREE fractionation). b) Eu anomaly ($\text{Eu}/\text{Eu}^* = \text{Eu}_{\text{norm}} (\text{Sm}_{\text{norm}} * \text{Gd}_{\text{norm}})^{0.5}$). c) Ce anomaly Ce/Ce^* ratios ($= \log \text{Ce}_{\text{norm}} / (\text{La}_{\text{norm}} + \text{Pr}_{\text{norm}})$).

conditions (subcycle 1g), the second one under oxidizing conditions (subcycle 3b/capped by erosion—see also Table 1).

5.2.3. Salinity variation

Ce and Eu anomalies do not correlate with changes in the depositional environment and have no meaning for the interpretation of the depositional environment. The redox regime in the depocentre has had no impact on the Ce anomaly of the fluids, either. Fractionation of LREE (La) and HREE (Lu) with regard to complexing ligands and their preferred partition have been studied by Bau and Möller (1992), Smith et al. (2000) and Kolonin and Shironosova (2002). Fluids with carbonate and halogen species as in the present case see fractions mainly controlled by complexing reactions. Hence the decreasing-upward trend among the La/Lu ratios is interpreted in terms of a change from high-salinity to low-salinity fluids (Fig. 10). The salinity increases in the sulfate- and dolomite-bearing sediments and shows low values in siliciclastic and organic sediments.

5.2.4. Physicochemical conditions and land-sea proximity indicators

Pyrite and hematite alone are insufficient to constrain the redox conditions by providing precise Eh values in volts. The element triplet Zn, Cu and Pb, however, offers a more subtle method to depict the redox regime at the transition from the evaporites into the OM-bearing facies. The base metals are arranged in order of increasing Eh values and proximity to land: Zn ($Eh \ll 0$) \Rightarrow Cu ($Eh \leq 0$) \Rightarrow Pb ($Eh \leq 0$). Zinc and lead which occur in nature only in the bivalent state have sharp peaks in the reducing and oxidizing regime, respectively. Copper which occurs in form of mono- and bivalent cations, consequently shows a “continuum”. No base metal sulfides were found and thus traces of Zn were held to be accommodated in the lattice of Fe disulfides. Cu is incorporated to some degree in disulfides, the remaining part is bound to Fe oxides and Pb bound to sulfide as well as carbonate minerals. This gradual change observed at the sea–land transition reflects different redox conditions and stages of mobilization. In a chemical–physical quiet regime (starved basin, coal swamp) base metals are fixed, fluvial drainage and fluctuating water tables conducted to a remobilization of elements along with an increase in the suspended load which in this case affected Cu and Pb more than Zn.

These findings in nature agree with laboratory experiments performed for these base metals (Brookins, 1987; Calmano et al., 1992). The pH values did not vary significantly and mostly lie at $pH \geq 7$ as indicated by the presence of carbonate and sulfate minerals. This is also indicated by the different species containing Fe, Cu, Zn and Pb. Precise pH-Eh figures may only be reported for the various subenvironments based on stability fields of hematite, malachite, smithsonite, cerussite, tenorite and cuprite (Fig. 11). This pH regime is not only valid for the chemical sediments but also for the detrital material where illite–smectite mixed layers are the only phyllosilicates present. Smectite developed off-shore in evaporite–carbonate sequences whereas kaolinite and illite settled near-shore (Dill et al., 2005). Moreover smectite formed under more alkaline conditions, whereas kaolinite is typical of more acidic pore fluids (Weaver, 1989). The yellow staining caused by some jarosite is due to present-day weathering (Fig. 4c).

5.2.5. Nutrient supply and state of aridity

All organisms on land and in the sea require phosphorus for synthesizing phospholipids, NADPH, ATP, nucleic acids, and other compounds. Plants absorb phosphorus, herbivores get phosphorus by eating plants and excreted phosphorus will be released into the soil. In the marine ecosystem upwelling is responsible for many of the world class phosphate deposits (Rusch et al., 1996; Dill and Kantor, 1997). The phosphate distribution is well-balanced throughout the entire sequence under study with highs in the siliciclastic beds and moderate values observed in the chemical and OM-bearing

sediments. In the sulfate-dolomite facies, phosphate covaries with the detrital component (Fig. 2a). Phosphorus I positively correlated with K and Ce attesting to monazite grains being delivered together with illite to the depocentre. In the dolomite–sulfate and silicate–coal facies, the phosphate dynamic in soil and the organic phosphate plays the dominant part in the basin. The availability of phosphate is affected by the soil pH. Reading the chemical signatures of the sediments at the passage from the dolomite–sulfate into the silicate–coal facies shows a sudden drop of non-detrital phosphate being flushed out. This wash-out process is caused by the hydraulic processes under changing wet-dry tropical conditions. The phosphate distribution is another measure for the aridity and hydraulic system on land and in the sea.

5.3. Organic chemofacies—Biogenic processes

The high S contents in the OM-bearing sediments argue for the availability of sulfate during coalification or in terms of hydrology for brackish or alkaline water (Casagrande, 1987). The samples at 26 m are characterized by high TOC contents, low extraction yields and high contents of resins arguing for the presence of refractory solid bitumen which formed through biotic and abiotic processes (Hunt, 1996).

High proportions of long-chain C_{27} – C_{31} *n*-alkanes relative to the sum of *n*-alkanes (Fig. 7) are typical of vascular plants, where they occur as the main components of plant waxes (Eglinton and Hamilton, 1967). The short-chain *n*-alkanes ($< C_{20}$), which are predominantly found in algae and microorganisms (Cranwell, 1977), are detected in higher amounts (> 20% of the total *n*-alkane concentrations) in the coalified matter and the black shale of the dolomite–sulfate facies. However, the distribution pattern of *n*-alkanes in the dolomite–sulfate facies may indicate a contribution of migrated bitumen. Taking into account the low abundance of the acyclic isoprenoids pristane (Pr) and phytane (Ph) in several of the samples, which resulted in considerable errors in peak integration (standard deviation in the range of ± 0.2 to 0.3), the Pr/Ph ratios (between 0.9 and 2.5; Table 4b) must be interpreted with care. According to Didyk et al. (1978), Pr/Ph ratios between 1.0 and 3.0 indicate dysaerobic conditions during early diagenesis, whereas values below 1.0 are considered to be indicative of anoxic conditions. However, Pr/Ph ratios are also known to be strongly affected by maturation (Tissot and Welte, 1984) and by differences in the precursors for acyclic isoprenoids (i.e. bacterial origin; Haven ten et al., 1987). In the present case, the influence of different ranks on Pr/Ph ratios can be ruled out, and an archaeal origin of phytane seems to be less favorable in such environments. In contrast, a high proportion of pristane may be derived from tocopherols (Goossens et al., 1984). The Pr/Ph values of the samples are interpreted to be consistent with anoxic to dysoxic conditions during early diagenesis. Higher Pr/Ph ratios in the dolomite–sulfate facies are in the range normally observed in terrestrial OM degraded under aerobic conditions. The lowest Pr/Ph ratio is found in the black shale sample consistent with its presumed deposition under anoxic conditions.

Algae are the predominant primary producers of C_{27} sterols, while C_{29} sterols are more typically associated with land plants (Volkman, 1986). However, numerous results from recent biomarker studies add to the growing list of microalgae that contain high proportions of 24-ethylcholesterol. The predominance of C_{29} steranes in most samples is consistent with an origin of OM from land plants. The high contents of C_{28} diasterenes in the lignite-jet maybe partly derived from algal or bacterial biomass or migrated into the jet. C_{30} 4-methylsteroids appear to be related to marine and lacustrine precursors (Peters and Moldowan, 1993). A higher contribution of algal OM is indicated by the steroids present in the black shale EOM. The ratio of the $20S/(20S+20R)$ isomers of the $5\alpha,14\alpha,17\alpha(H)-C_{29}$ steranes is between 0.24 and 0.30, far from the equilibrium value of 0.52 (Table 4b). This ratio correlates

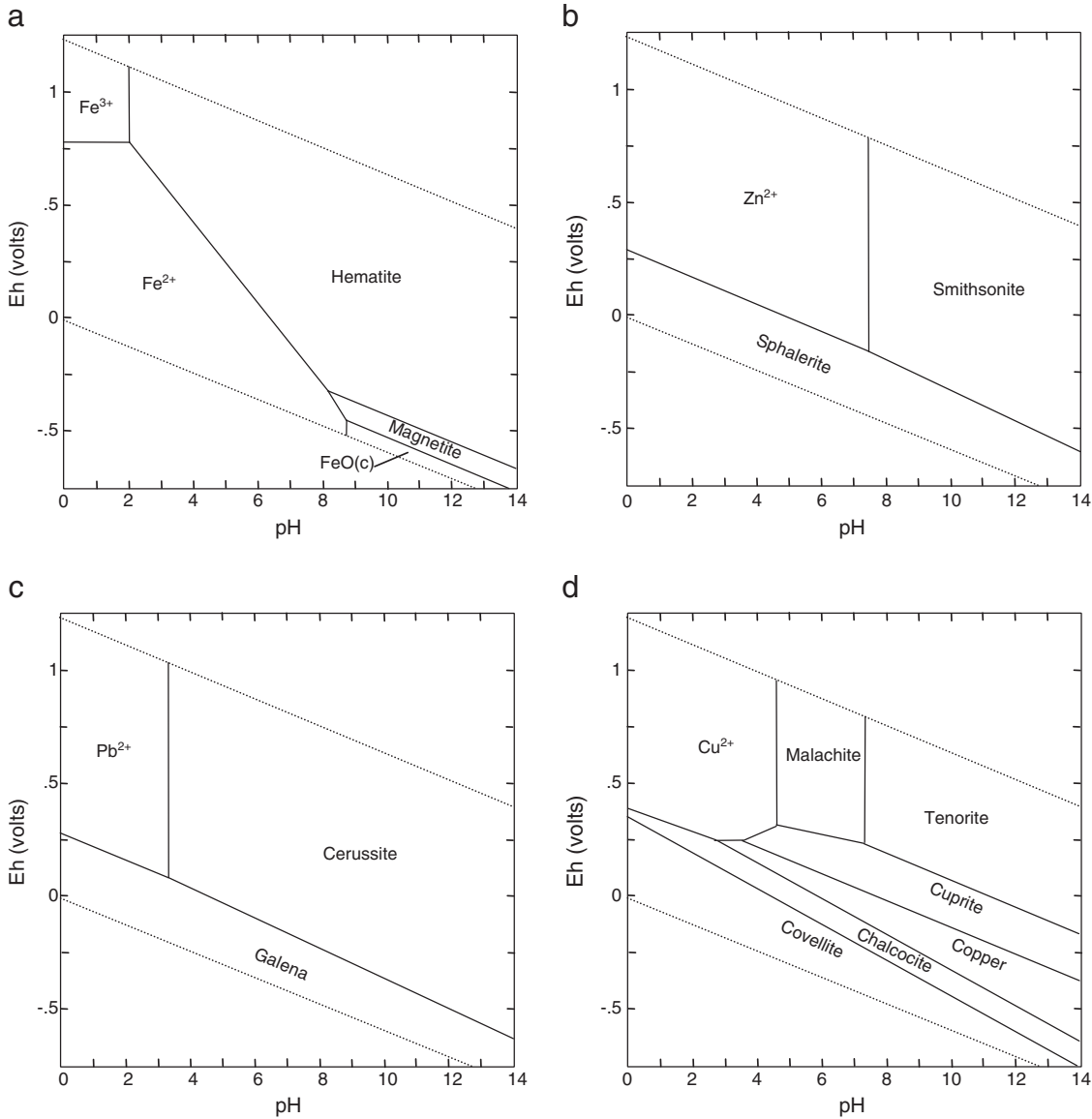


Fig. 11. Eh-ph diagrams to constrain the Eh-pH regime of the Abu Ruweis chemical and biogenic sediments. The most probable stability fields characterizing the Eh-pH regime are denoted by the marker minerals in each plot (e.g. hematite facies). Assumed concentrations of dissolved species are given below in mol/l. a) Eh-pH diagram to show the Fe mineralization at <50 °C using the dissolved species as $\log_{10} a_{\text{Fe}} = -6$. Hematite facies. b) Eh-pH diagram to show the Zn mineralization at <50 °C using the dissolved species as $\log_{10} a_{\text{Zn}} = -4$, $\log_{10} a_{\text{HCO}_3} = -3$, $\log_{10} a_{\text{HSO}_4} = -3$. Smithsonite-sphalerite facies. c) Eh-pH diagram to show the Pb mineralization at <50 °C using the dissolved species as $\log_{10} a_{\text{Pb}} = -8$, $\log_{10} a_{\text{HCO}_3} = -3$, $\log_{10} a_{\text{HSO}_4} = -3$. Cerussite-galena facies. d) Eh-pH diagram to show the Cu mineralization at <50 °C using the dissolved species as $\log_{10} a_{\text{Cu}} = -3$, $\log_{10} a_{\text{HCO}_3} = -2 \log_{10} a_{\text{SO}_4} = -3$. Malachite-tenorite-cuprite facies.

with a vitrinite reflectivity of 0.4–0.5% R_v (Mackenzie and Maxwell, 1981) higher than the measured reflectance values.

The most probable biological precursors of the hopanes are bacterialhopanepolyols (Rohmer et al., 1992). These compounds have been identified in aerobic bacteria and fungi, as well as in cryptogams (e.g. ferns, moss) and most recently, sulfate-reducing bacteria (Blumenberg et al., 2006). The ratio of the 22S/(22S + 22R) isomers of the 17 α ,21 α (H) C₃₁ hopanes of most samples (Table 4a) is in the range of 0.44 to 0.51 close to the equilibrium value of ca. 0.6 (Mackenzie et al., 1982). These values argue for a thermal maturity equivalent to vitrinite reflectance values of 0.4 to 0.5% R_v , as already proposed from the proportions of R/S isomers of the $\alpha\alpha\alpha$ -C₂₉ steranes (Mackenzie and Maxwell, 1981). The sesqui- and diterpenoids are most probably derived from precursor molecules abundant in leaf resins of conifers belonging to the Podocarpaceae, Araucariaceae, and Cupressaceae families (Otto and Wilde, 2001). Araucariaceae and Podocarpaceae evolved during the Early Triassic and are, therefore,

considered as the most probable precursor plants for the sesqui- and diterpenoids found in the EOM of the samples (Stewart, 1983).

Phenanthrene and its methylated analogues derived from a variety of non-specific precursor compounds such as steroids and triterpenoids (Tissot and Welte, 1984). Polycyclic aromatic hydrocarbons (PAHs) with 4–5 rings ranging from fluoranthene to benz-(ghi)-perylene are present in the samples (Fig. 8). In recent sediments combustion products of fossil fuels represent the main source of these PAHs (Laflamme and Hites, 1978). PAHs in ancient sediments may result from wildfires (Killops and Killops, 1993), or may be formed during microbially mediated diagenetic processes (Alexander et al., 1992). Some compounds may have originated from polyaromatic precursors which were synthesized by living organisms as for instance fungi (Tissot and Welte, 1984). As charcoal is part of the sample set (Fig. 8), the PAHs present in the samples and the absence of their methylated analogues, argue for the origin of these compounds from charcoal and/or an input of PAHs attributed to recurring forest

or swamp fires triggered by thunderstorm. However, as outcrop samples are investigated, an anthropogenic source (i.e. combustion products of fossil fuels) cannot be excluded. The presence of oxygenated PAH components (e.g. dibenzofuran; (Fig. 8) is in agreement with this interpretation, as these compounds are attributed to an origin from charcoal. Beside these PAHs, S-containing compounds (e.g. dibenzothiophene) argue for the incorporation of S into the OM in a high-S environment and their formation during maturation (Sinnighe Damsté and de Leeuw, 1990)—(see also sulfur isotopes).

5.4. Isotopic chemofacies—Diagenetic to epigenetic alteration

The O isotope values of bulk carbonate samples have been used to estimate formation temperatures of the carbonate fraction of the sediments. Formation temperatures were calculated by using the thermodynamic equilibrium equation of O'Neil et al. (1969) and sea water (except the topmost sample where we used the meteoric water isotope value). Marine reference data were used to calculate the temperature of formation, as the calcareous rocks reflect the marine incursion as well as diagenetic alteration caused by sea water. Achieved temperatures for all samples are rather uniform near 50 °C (Fig. 9a). It seems that the carbonate fraction formed at rather low temperature most likely well below 100 °C.

The overall thickness of the hanging wall Jurassic series on top of the Abu Ruweis Fm. may be deduced from Table 1. Another 300 m of Cretaceous sediments have to be added to the 420 m measured for the Jurassic sediments. The temperature determined for the post-depositional alteration is much higher than expected for a series measuring approximately 800 m and subjected to simple late burial diagenesis. The elevated temperature of as much as 100 °C determined for the diagenetic to epigenetic alteration argues for some heat provided by rifting processes along the Dead-Sea Transform Fault (Fig. 1b). Carbonate and clastic deposits in prodelta and delta front settings show fluctuating temperatures of formation between 48 °C to 60 °C due to highly variable diagenetic features such as different porosity and permeability characteristics which govern the flow and transfer of heat (Fig. 2b). The C isotopes of the bulk carbonates have negative δ-values between –3.9 and –12.4‰. The values decrease from bottom to the 20 m depth interval and then increase again to less negative values. Negative C isotope values of carbonates indicate a biogenic ¹²C-rich carbon source which is admixed to sea water bicarbonate (near 0‰).

The isotope composition of the sulfide fraction in the claystones and marls (–24.0 to –28.9‰) of the sulfate-dolomite facies is typical of sulfides formed by bacterial sulfate reduction. On the other hand, the δ³⁴S of the sulfate extracted from the same samples and from similar lithologies of the dolomite-sulfate facies ($\delta^{34}\text{S} = +7.5$ to +11.6‰) is depleted relative to connate seawater sulphate and is consistent with the isotope composition of sulfate formed in a playa lake or sabkha environment (Alonso-Azcarate et al., 2006; Elias et al., 2007). The observed range of δ values can be explained by a mixture of marine sulfate and isotopically relatively light sulfur derived from continental sources which may have formed e.g., by re-oxidation of sulfides, by dissolution of earlier, low δ³⁴S evaporites (e.g., Zechstein evaporites) or from precipitation/atmospheric fallout (Eckardt and Spiro, 1999; Berner et al., 2002). The sequence of δ³⁴S values recorded in the evaporitic gypsum-bearing layers correspond to dissolved sulfate modified by progressive evaporation in a playa lake, as suggested by the isotopic evaporation experiments of Raab and Spiro (1991). The slight decrease in the lower part of the Abu Ruweis Fm. could reflect a reservoir effect which may develop in a closed or partially closed marginal basin in which the residual brine is gradually depleted in ³⁴S due to the slight fractionation of the S isotopes during gypsum precipitation. A further evaporation inverts the trend, and in the Mg-sulfate and K-Mg-sulfate fields, the δ³⁴S of the brines becomes higher than that of the precipitates (Raab and Spiro, 1991).

5.5. Coal facies—Environment of deposition and coalification

The presence of textinates A and B points to lignified vascular bundles and primary woody fragments. Based on the size, it is likely that the wood fragments formed from tree trunks, branches or thick roots. The high degree of cell-tissue preservation attests dry conditions within forested peatlands or raised bogs (Diessel, 1992).

The crassi-cutinite represents lower-leaf assemblages. The presence of distinct and thick intercellular flanges of the epidermal cells implies that the leaves pertain to the evergreen plants. The lack of thick and well-developed outer walls of the guard cells is indicative of gymnosperm taxa. The nipple-like projections of irregularly occurring cells surrounding the guard cells reflect attachments for hair-like outgrowths (trichomes) of possibly ferns (Upchurch, 1995).

Hite and Anders (1991) supported the lack of vitrinite suppression in coal samples completely embedded in halite and displaying equivalent Rr values according to the linear plots of vitrinite reflectance vs. depth. However, the lack of suppression of ulminite reflectance in host rocks belonging to a carbonate–halite facies contradicts this opinion as to a reflectance suppression in marine carbonate rocks (Bostick and Foster, 1975) and lacustrine carbonate rocks (Hite and Anders, 1991).

Entering the reflection data from Table 2 into the equation put forward by Barker and Pawlewicz (1986) ($T = (\ln(Rr) + 1.68)/0.0124$) provides an approximation of the maximum paleotemperature during diagenesis. Our data yield a maximum paleotemperature of 100.7 °C for the black shale and of 74.6 °C for the coal samples. The difference in the thermal maturity in our samples point to a random vitrinite reflectance, excluding the elevated thermal maturity, i.e., 0.65% Rr in the black shales. Oxidation or desiccation processes during deposition and prior to accumulation could account for this slightly higher maturity in the black shales (Hagemann and Wolf, 1989).

5.6. Synopsis—The depositional environment of the “Arabian Keuper Facies” its economic potential and geodynamic setting

The analyses of the chemical, mineralogical and organic facies indicate an epicontinental depositional environment with some short-lasting marine transgressions (Fig. 2b). The continental basin barred from the open sea of the Tethys Ocean shows a gradual deepening, a slowing down of aridity and evaporation and so does the sedimentary influx. Following the facies models for evaporites put forward by Warren (2006), subcycles 1a through 1d are interpreted in terms of salinas or playas with ephemeral lacustrine deposits at the basin center and evaporitic mud flats at the edge. These mixed carbonate–siliciclastic deposits prograded onto sulfate deposits as the continental run-off increased. It was a rather shallow basin, with a shallow brine level. Subcycles 1e and part of 1g saw the basin deepening with some minor marine transgressions from the open sea reaching into the lagoon. The brine level was still low while the basin was deepening. The salinas gradually converted into salters. Oversteepening of the paleoslope in the basin triggered slumping within the evaporitic–siliciclastic series (Fig. 3d). The Abu Ruweis Fm. is a regressive, mixed carbonate–siliciclastic unit, featuring the progradation of a delta similar to the active Mahakam Delta in east Borneo, SE Asia in a tropical region (Wilson and Lokier, 2002; Hook and Wilson, 2003). Clastic sedimentation onto the shallow shelf eliminated sulfate precipitation and inhibited carbonate production. Prodella and delta front deposits still contain significant amounts of sulfate and dolomite in a tidal dominated regime (Fig. 2b). The delta plain represented by subcycles 3a and 3b are dominated by the detrital fluvial input. During episodes of relative tectonic quiescence OM was accumulated in swamps and poorly aerated parts of the delta plain (wet fan). In the more landward red beds, typical oxisols developed on top of the coal swamps (Fig. 4a, b, c, d).

Sedimentary influx at this time was almost nil leading to what might be called a "starved basin" under restricted marine conditions. Continental ground water flow was much lower than the episodic overflow from the sea which was stopped at the passage from the sulfate–dolomite into the dolomite–sulfate facies. Temperatures derived from O isotopes analyses and OM show the same trend but the OM reflects a constantly higher temperature regime. Obviously the OM responded more sensitively to temperature changes than the carbonate minerals. The abnormally high T-values at the passage from the sulfate–dolomite into the dolomite–sulfate facies correlate with a restricted marine environment abundant in pyrite and Zn. This high heat flow is correlated with Middle Triassic rifting processes in the Tethys leading in the Alps to MVT-Zn-Pb deposits in Austria, Slovenia, and Italy (Dill et al., 2008). Even outside the Tethys ocean Anisian (Middle Triassic) and late Norian (Late Triassic) rifting gave rise to Zn-Pb deposits, e.g., in the Alexander Terrane in Southeastern Alaska and Northwestern British Columbia (Dill et al., 2008; Taylor et al., 2008). Fluid inclusion studies attest to biogenic sulfur in the base metal sulfides and constrain the temperatures of formation to the T range 100–200 °C (Kuhlemann, 1995; Schroll and Prochaska, 2004). In terms of economic geology the gypsum–dolomite–celestite deposits may be coded 31d KL *sensu* Dill (2010). They are economic for the exploitation of calcium sulfate but subeconomic as to celestite. Towards the open sea even halite may enter the spectrum of evaporite minerals and become an economic mineral in what may be coded as 35a L deposit *sensu* Dill (2010). This situation is represented in Central Europe and Jordan where gypsum-bearing seams form the basis for a flourishing gypsum industry near Würzburg, Germany, while halite deposits occur in eastern France in the same stratigraphic unit (Dill et al., 2008). Passing more landward with the salinas turning into evaporitic mudflats, celestite plus celestobaryte tend to prevail over anhydrite/gypsum. As a consequence Sr–Ba deposits of the "Eyre-type" 34b J come into existence (Dill, 2010). The lignite seams of Abu Ruweis Fm. are not productive in the area under study.

The current study focuses on a passive margin basin along the southern edge of the Neo-Tethys Ocean, encroaching upon the Arabian Platform. Detailed stratigraphic and cyclic subdivisions allow for a basinwide correlation of the Abu Ruweis Fm. with other sedimentary units in this area which developed in a post-rift geodynamic setting (Sharland et al., 2001): Bakuk Fm., Turkey; Kurra Chine Fm., Iraq, Dashtak Fm., Iran, Gulailah-D Fm., United Arab Emirates, Jilh Fm. Oman. The "Arabian Keuper Facies" is transitional between the "Germanic Keuper Facies" typical of epicontinental basins with no hydrothermal activity and the "Alpine Triassic Facies" of the Tethyan Ocean or, in general, mobile crustal zones, where hydrothermal submarine activity is common. The salinity decrease, inferred from the REE distribution, along with a change from the evaporitic into the OM-dominated facies is the most pronounced feature of the chemofacies of "Arabian Keuper Facies".

6. Summary and conclusions

The inorganic, organic and isotope-based chemofacies analysis of the Abu Ruweis Fm. in context with the mineralfacies and coal facies analyses allow for the definition of a special geodynamic facies called the "Arabian Keuper Facies". The reference type of this evaporite-coal facies, which is Carnian (Late Triassic) in age, is located in NW Jordan. This facies translates into a geodynamic setting transitional between the fully marine "Alpine Triassic Facies" of the Tethyan Ocean, hosting MVT Pb-Zn deposits, and the epicontinental "Germany Keuper Facies" which is separated from the Tethys Ocean and lacking any hydrothermal activity as well as major marine ingressions. Similar facies types developed at the same time in Poland, Croatia, and Germany. Not of the same age but similar with regard to the depositional

environment, the Purbeck–Wealden facies in southern England may be held also equivalent to the facies under study.

Strong evaporation in the series is demonstrated by the presence of dolomite, gypsum and celestite. Mg, Ca, F, Cl, S, Sr and Ba are the most suitable marker elements for the rate of evaporation. Salinity variation may be characterized as its best by the fractionation of LREE (La) and HREE (Lu). Complexing ligands and sorption processes govern the variation of La/Lu ratios.

The detrital influx is characterized by the abundance of Si, Ti, Al, Fe, Mn Ce, Co, Cr, V, Y and Zr. The most suitable parameter to mark the high detrital input is the (Zr + Rb)/Sr ratio.

Pyrite and hematite are the only redox markers in these sediments and useful as a land-sea proximity indicator. The element triplet Zn, Cu and Pb, however, offers a clue to the redox regime and support the mineralogical-based proximity indicators: Zn ($Eh \ll 0$) \Rightarrow Cu ($Eh \leq 0$) \Rightarrow Pb ($Eh \leq 0$).

The C isotopes of the carbonate fractions indicate biogenic CO_2 admixed to the marine-derived pore water bicarbonate (with $\delta^{13}C$ near 0‰) during early diagenesis. Organic degradation processes such sulfate reduction probably produced the ^{12}C -enriched organic CO_2 . Based on the O isotope variations we calculated relatively low and uniform formation temperatures near 50 °C for the bulk carbonates. The elevated thermal gradient argues for some heat provided by rifting processes along the Dead-Sea Transform Fault. Temperature data obtained during coal petrography yielded maximum paleotemperatures of 100 °C for the black shale and about 70 °C for the coal samples. The latter are likely to reflect small-scale hot brine activity in the basin but without any metalliferous impact in form of MVT deposits on the stratigraphy.

Carbon isotopes show an admixture of OM to the build up of the carbonates during early diagenesis. The isotope composition of sulfides in shales and marls is typical of sulfides formed by bacterial sulfate reduction, while in addition to sulfate precipitated from evaporitic brines, some sulfate resulted from later re-oxidation of the sulfides.

Detrital phosphorus I is bound to monazite. All organisms on land and in the sea require phosphorus for synthesizing phospholipids, NADPH, ATP and nucleic acids (phosphorus II).

The high sulfur contents in the coal-bearing sediments are interpreted in terms of brackish or alkaline waters.

Long-chain C_{27} – C_{31} *n*-alkanes are typical of vascular plants. The short-chain *n*-alkanes ($<C_{20}$) are predominantly found in algae and microorganisms. The acyclic isoprenoids pristane (Pr) and phytane (Ph). Pr/Ph ratios between 1.2 and 2.5 indicate dysaerobic conditions during early diagenesis. The ratio of the $20S/(20S + 20R)$ isomers of the $5\alpha,14\alpha,17\alpha(H)-C_{29}$ steranes is between 0.24 and 0.30 and correlates with a vitrinite reflectivity of 0.4–0.5% R_v . The sesquiterpenoids and diterpenoids are most probably derived from precursor molecules abundant in leaf resins of conifers. Phenanthrene and its methylated analogues derived from combustion products of fossil fuels. Among the maceral types, textinit A and B represent xylem features of tree trunks and the crassi-cutinit upper leaf cuticles.

The paleogeographic setting of the "Arabian Keuper Facies" is characterized by a transgressive subfacies followed by a regressive subfacies. Two cyclic units with salinas (salt pan/playa) at the base and prograding mudflats on top reflect a gradual deepening of the basin. The third salina cycle faded out in a marine incursion and reworking of sulfate. The turning point from a transgressive towards a regressive facies is marked by a restricted marine depositional environment when the ultimate depth was reached within the "Arabian Keuper Basin". Mud-laden rivers that reached this standing water body carried a significant amount of siliciclastic material which they dumped in form of a prodelta gradually converting into delta front sands as the grain size and the amount of siliciclastic material increased. The basin subsidence diminished and arenaceous sediments came to rest within a delta front and delta plain depositional

environment. Shallowing of the basin provoked poorly aerated swamps to turn into well aerated delta plains where paleosols and coal seams eventually developed. The gradual transition from continental sulfate-bearing cycles of evaporites into sulfide-bearing carbonaceous beds with a minor marine incursion at the reversal of these facies is held to be diagnostic for the "Arabian Keuper Facies".

Supplementary materials related to this article can be found online at doi:10.1016/j.chemgeo.2011.12.028.

Acknowledgements

We are indebted to F. Korte for doing the chemical analyses with XRF, D. Klosa for SEM analyses, and D. Weck who performed the XRD analyses. All investigations were carried in the laboratories of the Federal Institute for Geosciences and Natural Resources in Hannover, Germany, the Department of Applied Geosciences and Geophysics, University of Leoben, Austria. Isotope analyses were performed at the Institute for Mineralogy and Geochemistry at the Karlsruhe Institute of Technology (G. Preus) and at the Geological-Paleontological Department of the University Kiel, Germany. The senior author would like to express his gratitude to the German Academic Exchange Service (DAAD) who provided a financial grant for his stay at Amman, Jordan. The senior author would like to thank his friends from the Geological Department for their support during his stay as a visiting professor at the University of Jordan. We would like to thank an anonymous reviewer and Andrew Horbury for their comments to a first draft of our paper and Uwe Brand for his editorial handling of our paper.

References

- Abu Hamad, A., 1994. Stratigraphy and Microfacies of The Triassic in Wadi Abu Oneiz Area (West Na'ur). Unpubl. M. Sc. Thesis. Dep. of Earth Science. Yarmouk University, Irbid, Jordan.
- Adams, J.J.A., Weaver, C.E., 1958. Th-to-U ratios as indicators of sedimentary process—an example of geochemical facies. American Association of Petroleum Geologist Bulletin 42, 387–430.
- Alexander, R., Larcher, A.V., Kagi, R.I., Price, P.L., 1992. An oil-source correlation study using age specific plant-derived aromatic biomarkers. In: Moldowan, M.J., Albrecht, P., Philip, P.R. (Eds.), *Biological Markers in Sediments and Petroleum*. Prentice-Hall, Englewood Cliffs, NJ, pp. 201–221.
- Alonso-Azcarate, J., Bottrell, S.H., Mas, J.R., 2006. Synsedimentary versus metamorphic control of S, O and Sr isotopic compositions in gypsum evaporites from the Cameros Basin, Spain. Chemical Geology 234, 46–57.
- Andrews, I., Makhlouf, I., Taani, Y., Al-, Bashish, Al-Hiayari, A., 1992. Permian, Triassic and Jurassic lithostratigraphy in the subsurface of Jordan. Subsurface Geology Division. Geology Directorate. : Bulletin, 4. NRA, Amman.
- Bandel, K., 1981. New stratigraphical and structural evidence for lateral dislocation in the Jordan Rift connected with a description of the Jurassic rock column in Jordan. Neues Jahrbuch Geologie Paläontologie Abhandlungen 161, 271–308.
- Bandel, K., Khoury, H., 1981. Lithostratigraphy of the Triassic in Jordan. Facies 4, 1–26.
- Barker, C.E., Pawlewick, M.J., 1986. Concentration of dispersed sedimentary OM for vitrinite reflectance analysis using a simple crush and float method. Society of Organic Petrology Newsletter 3, 3.
- Bau, M., Möller, P., 1992. Rare earth element fractionation in metamorphogenic hydrothermal calcite, magnesite and siderite. Mineralogy and Petrology 45, 231–246.
- Bender, F., 1974. Geology of Jordan. Gebrüder Borntraeger, Stuttgart. 196 pp.
- Berner, Z., Stüben, D., Leosson, M., Beushausen, M., Klinge, H., 2002. S- and O-isotopy of dissolved sulfate in the cover rock aquifer of a Permian salt dome. Applied Geochemistry 17, 1515–1528.
- Bhatia, M.R., Cook, K.A.W., 1986. Trace element characteristics of greywackes and tectonic setting discrimination of sedimentary basins. Contributions to Mineralogy and Petrology 92, 181–193.
- Blumenberg, M., Krüger, M., Nauhaus, K., Talbot, H.M., Oppermann, B.I., Seifert, R., Pape, T., Michaelis, W., 2006. Biosynthesis of hopanoids by sulfate-reducing bacteria (genus *Desulfovibrio*). Environmental Microbiology 8, 1220–1227.
- Bostick, N.H., Foster, J.N., 1975. Comparison of vitrinite reflectance in coal seams and in kerogen of sandstones, shales and limestones in the same part of a sedimentary section. In: Alpern, B. (Ed.), *Petrographie Organique et Potentiel Petrolifère*. Centre National de la Recherche Scientifique, Paris, pp. 13–25.
- Bray, E.E., Evans, E.D., 1961. Distribution of n-paraffins as a clue to recognition of source beds. Geochimica et Cosmochimica Acta 22, 2–15.
- Brookins, D.G., 1987. Eh-pH Diagrams for Geochemistry. Springer, Heidelberg. 176 pp.
- Calmano, W., Hong, J., Förster, U., 1992. Einfluß von pH-Wert und Redox-Potential auf die Bindung und Mobilisation von Schwermetallen in kontaminierten Sedimenten. Vom Wasser 78, 245–257.
- Casagrande, D.J., 1987. Sulfur in peat and coal. In: Scott, A.C. (Ed.), *Coal and Coal-Bearing Strata: Recent Advances*. Geological Society, London, Special Publication, 32, pp. 87–105.
- Cox, R., Lowe, D.R., Cullers, R.L., 1995. The influence of sediment recycling and base metal composition on evolution of mudrock chemistry in the southwestern United States. Geochimica et Cosmochimica Acta 59, 2919–2940.
- Cranwell, P.A., 1977. Organic geochemistry of CamLoch (Sutherland) sediments. Chemical Geology 20, 205–221.
- Dean, W.E., Arthur, M.A., 1998. Geochemical expressions of cyclicity in Cretaceous pelagic limestone sequences: Niobrara Formation, Western Interior Seaway. SEPM Concepts in Sedimentology and Paleontology 6, 227–255.
- Didyk, B.M., Simoneit, B.R.T., Brassell, S.C., Eglington, G., 1978. Organic geochemical indicators of paleoenvironmental conditions of sedimentation. Nature 272, 216–222.
- Diessel, C.F.K., 1992. Coal-bearing Depositional Systems. Springer, New York. 721 pp.
- Dill, H.G., 2010. The "chessboard" classification scheme of mineral deposits: mineralogy and geology from aluminum to zirconium. Earth-Science Reviews 100, 1–420.
- Dill, H.G., Kantor, W., 1997. Depositional environment, chemical facies and a tentative classification of some selected phosphate accumulations. Geologisches Jahrbuch D 105, 3–43.
- Dill, H.G., Botz, R., Berner, Z., Stüben, D., Nasir, S., Al-Saad, H., 2005. Sedimentary facies, mineralogy and geochemistry of the sulfate-bearing Miocene Dam Formation in Qatar. Sedimentary Geology 174, 63–96.
- Dill, H.G., Wehner, H., Kus, J., Botz, R., Berner, Z., Stüben, D., Al-Sayigh, A., 2007. The Eocene Rusayl Formation, Oman, carbonaceous rocks in calcareous shelf sediments: environment of deposition, alteration and hydrocarbon potential. International Journal of Coal Geology 72, 89–123.
- Dill, H.G., Sachsenhofer, R.F., Grecula, P., Sasvári, T., Palinkaš, L.A., Borojević-Šoštaric, S., Strmić-Palinkaš, S., Prochaska, W., Garuti, G., Zaccarini, F., Arbouille, D., Schulz, H.-M., 2008. Fossil fuels, ore—and industrial minerals. In: McCann, T. (Ed.), *Geology of Central Europe*. Geological Society of London, Special Publication, London, pp. 1341–1449.
- Dypvik, H., Harris, N.B., 2001. Geochemical facies analysis of fine-grained siliciclastics using Th/U, Zr/Rb and (Zr+Rb)/Sr ratios. Chemical Geology 181, 131–146.
- Eckardt, F.D., Spiro, B., 1999. The origin of sulfur in gypsum and dissolved sulfate in the Central Namib Desert, Namibia. Sedimentary Geology 123, 255–273.
- Eglington, G., Hamilton, R.J., 1967. Leaf epicuticular waxes. Science 156, 1322–1335.
- Elias, A.D., De Ros, L.F., Mizusaki, A.M., Koji Kawashita, K., 2007. Isotopic evidence on the diagenetic evolution of coastal sabkha reservoirs from the Solimões Basin, northern Brazil. Gondwana Research 11, 553–567.
- Galloway, W.E., Hobday, D.K., 1996. *Terrigenous Clastic Depositional Systems—Applications to Fossil Fuel and Groundwater Resources*. Springer, Heidelberg. 484 pp.
- Goossens, H., de Leeuw, J.W., Schenck, P.A., Brassell, S.C., 1984. Tocopherols as likely precursors of pristane in ancient sediments and crude oils. Nature 312, 440–442.
- Hagemann, W.-H., Wolf, M., 1989. Paleoenvironments of lacustrine coals—the occurrence of algae in humic coals. International Journal of Coal Geology 12, 511–522.
- Hamrla, M., 1959. On the conditions of origin of the coal beds in the Karst region (in Slovenian). Geologija 1959, 180–264.
- Haven ten, H.L., de Leeuw, J.W., Rulkötter, J., Sinninge Damsté, J.S., 1987. Restricted utility of the pristane/phytane ratio as a palaeoenvironmental indicator. Nature 330, 641–643.
- Hite, R.J., Anders, D.E., 1991. Petroleum and evaporites. In: Melvin, J.L. (Ed.), *Evaporites, Petroleum, and Mineral Resources*. Elsevier Scientific Pub. Co., New York, pp. 349–411.
- Hook, J., Wilson, M.E.J., 2003. Stratigraphic relationships of a Miocene mixed carbonate-siliciclastic interval in the Badak field, East Kalimantan, Indonesia. Proceedings of the 29th Indonesian Petroleum Association, pp. 398–412.
- Hunt, J.M., 1996. *Petroleum Geochemistry and Geology*. W.H. Freeman, New York.
- International Committee for Coal and Organic Petrology (ICCP), 1998. The new vitrinite classification (ICCP System 1994). Fuel 77, 349–358.
- International Committee for Coal and Organic Petrology (ICCP), 2001. The new inertinite classification (ICCP System 1994). Fuel 80, 459–471.
- Kalkreuth, W.D., 2004. Coal facies studies in Canada. International Journal of Coal Geology 58, 23–30.
- Khalil, B., Muneizel, S., 1992. Lithostratigraphy of the Jurassic Outcrops of North Jordan (Azab Group). Geological Mapping Division Bulletin, 21. Geology Directorate, NRA, Amman.
- Killops, S.D., Killops, V.J., 1993. An introduction to organic geochemistry. Longman Group, England, p. 265.
- Koch, G., 1998. *Palinostratigrafija Triajaskih Naslaga Hrvatskog Jadranskog Podmorja*. Ph.D. thesis University of Zagreb, 291 pp.
- Kolonin, G.R., Shironosova, G.P., 2002. Thermodynamic model for REE complexation in the course of interaction between REE-fluorite and hydrothermal fluid. Geochemical International 40, 103–112.
- Kuhlemann, J., 1995. Zur Diagenese des Karawanken-Nordstammes (Österreich/Slowenien): Spättriassische, epigenetische Blei-Zink-Vererzung und mitteltertiäre, hydrothermale Karbonatzentration. Archiv für Lagerstätteneorschung der Geologischen Bundesanstalt 18, 57–116.
- Laflamme, R.E., Hites, R.A., 1978. The global distribution of polycyclic aromatic hydrocarbons in recent sediments. Geochimica et Cosmochimica Acta 42, 289–303.
- Liu, G., Yang, P., Peng, Z., Chou, C.-L., 2004. Petrographic and geochemical contrasts and environmentally significant trace elements in marine-influenced coal seams, Yanzhou mining area, China. Journal of Asian Earth Sciences 23, 491–506.
- Longinelli, A., Flora, O., 2007. Isotopic composition of gypsum samples of Permian and Triassic age from the north-eastern Italian Alps: palaeoenvironmental implications. Chemical Geology 245, 275–284.
- Mackenzie, A.S., Maxwell, J.R., 1981. Assessment of thermal maturation in sedimentary rocks by molecular measurements. In: Brooks, J. (Ed.), *Organic maturation studies and fossil fuel exploration*. Academic Press, London, pp. 239–254.

- Mackenzie, A.S., Brassell, S.C., Eglington, G., Maxwell, J.R., 1982. Chemical fossils: the geological fate of steroids. *Science* 217, 491–504.
- Makaske, B., 2001. Anastomosing rivers: a review of their classification, origin and sedimentary products. *Earth-Science Reviews* 53, 149–196.
- Makhoul, I.M., 1998. Facies analysis of the Triassic Ain Musa Formation, Dead Sea, Jordan. *Abhath Al-Yarmouk* 7 (2), 150–165.
- Makhoul, I.M., 1999. Shallowing-upward facies of the Triassic Hisban Limestone Formation in Jordan. *Journal of Al-Manarah* 4 (2), 259–274.
- Makhoul, I.M., Turner, B.R., Abed, A.M., 1990. Depositional facies and environments in the Lower Triassic Ma'in Formation, Dead Sea Area, Jordan. *Dirasat, Series B* 17 (2), 7–26.
- McCrea, J.M., 1950. The isotope chemistry of carbonates and a paleotemperature scale. *Journal of Chemical Physics* 18, 849–957.
- McLennan, S.M., 1989. Rare earth element in sedimentary rocks: Influence of provenance and sedimentary processes. In: Lipin, B.R., McKay, G.A. (Eds.), *Geochemistry and Mineralogy of Rare Earth Elements*, vol. 21. Mineral Society of America, pp. 169–200.
- Moore, T.A., Shearer, J.C., 2003. Peat/coal type and depositional environment—are they related? *International Journal of Coal Geology* 56, 233–252.
- NCJSC, 2000. Nomenclature Committee for the Jordanian Stratigraphic Column. Part 2—Internal Report. NRA, Amman, pp. 1–46.
- O'Neil, J.R., Clayton, R.N., Mayeda, T.K., 1969. Oxygen isotope fractionation in divalent metal carbonates. *Journal Chemical Physics* 51, 5547–5558.
- Orłowska-Zwolinska, T., 1983. Palynostratigraphy of the upper part of Triassic epicontinent sediments in Poland. *Prace Instytutu Geologicznego* 104, 1–89 (Polish with English abstract).
- Otto, A., Wilde, V., 2001. Sesqui-, di-, and triterpenoids as chemosystematic markers in extant conifers—a review. *The Botanical Review* 67, 141–238.
- Peters, K.E., Moldowan, J.M., 1993. The Biomarker Guide: Interpreting Molecular Fossils in Petroleum and Ancient Sediments. Prentice-Hall, Englewood Cliffs, NJ, p. 154.
- Philp, R.P., 1985. Fossil fuel biomarkers. Applications and spectra. *Methods in Geochemistry and Geophysics* 23, 1–294.
- Raab, M., Spiro, B., 1991. Sulfur isotopic variations during seawater evaporation with fractional crystallization. *Chemical Geology* 86, 323–333.
- Radke, M., Willsch, H., Welte, D.H., 1980. Preparative hydrocarbon group type determination by automated medium pressure liquid chromatography. *Analytical Chemistry* 52, 406–411.
- Rohmer, M., Bisseret, P., Neunlist, S., 1992. The hopanoids, prokaryotic triterpenoids and precursors of ubiquitous molecular fossils. In: Moldowan, J.M., Albrecht, P., Philp, R.P. (Eds.), *Biological Markers in Sediments and Petroleum*. Prentice Hall, Englewood Cliffs, NJ, pp. 1–17.
- Rusch, T.L., Sankar, R., Scharf, J.E., Follmi, K.B., 1996. The phosphorus cycle, phosphogenesis and marine phosphate-rich deposits. *Earth-Science Reviews* 40, 55–124.
- Schroll, E., Prochaska, W., 2004. Contribution to ore fluid chemistry of Bleiberg Pb–Zn deposit (Austria) and affiliated deposits. Abstract band, 3.6.P05. Goldschmidt Geochemistry, Copenhagen, Denmark. 5 to 11 June 2004, A306.
- Shao, L., Jones, T., Gayer, R., Dai, S., Li, S., Jiang, Y., Zhang, P., 2003. Petrology and geochemistry of the high-sulfur coals from the Upper Permian carbonate coal measures in the Heshan Coalfield, southern China. *International Journal of Coal Geology* 55, 1–26.
- Sharland, P.R., Archer, R., Casey, D.M., Davies, R.B., Hall, S.H., Heward, A.P., Horbury, A.D., Simmons, M.D., 2001. Arabian Plate Sequence stratigraphy. *GeoArabia, Special Publication* 2, 1–371.
- Simoneit, B.R.T., Mazurek, M.A., 1982. OM of the troposphere—II. Natural background of biogenic lipid matter in aerosols over the rural western United States. *Atmospheric Environment* 16, 2139–2159.
- Sinnige Damsté, J.S., de Leeuw, J.W., 1990. Analysis, structure and geochemical significance of organically-bound sulfur in the geosphere: state of the art and future research. *Organic Geochemistry* 16, 1077–1101.
- Smith, M.P., Henderson, P., Campbell, L.S., 2000. Fractionation of the REE during hydrothermal processes. Constraints from the Bayan Obo Fe-REE-Nb deposit, Inner Mongolia, China. *Geochimica et Cosmochimica Acta* 64, 3141–3160.
- Stewart, W.N., 1983. *Palaeobotany and the evolution of plants*. Cambridge University Press, Cambridge, p. 348.
- Taylor, C.D., Premo, W.R., Meier, A.L., Taggart Jr., J.E., 2008. The metallogeny of Late Triassic rifting of the Alexander Terrane in Southeastern Alaska and Northwestern British Columbia. *Economic Geology* 103, 89–115.
- Teichmüller, M., 1989. The genesis of coal from the point of view of coal petrology. *International Journal of Coal Geology* 12, 1–87.
- Thomas, L., 2002. *Coal Geology*. John Wiley & Sons, New York. 384 pp.
- Tissot, B.T., Welte, D.H., 1984. *Petroleum Formation and Occurrences*, 2nd edition. Springer Verlag, Berlin. 699 pp.
- Toloczyki, M., Trurnit, P., Voges, A., 1999. International Geological Map of Europe and the Mediterranean Regions 1:1 500 000, Map Sheet F 7 Amman. Federal Institute for Geosciences and Raw Materials, Hannover.
- Upchurch Jr., G.R., 1995. Dispersed angiosperm cuticles: their history, preparation, and application to the rise of angiosperms in Cretaceous and Paleocene coals, southwestern interior of North America. *International Journal of Coal Geology* 28, 161–227.
- Volkman, J.K., 1986. A review of sterol markers for marine and terrigenous OM. *Organic Geochemistry* 9, 83–99.
- Waldron, J.W.F., Rygel, M.C., 2005. Role of evaporite withdrawal in the preservation of a unique coal-bearing succession: Pennsylvanian Joggins Formation, Nova Scotia. *Geology* 33, 337–340.
- Warren, J.K., 2006. *Evaporites:Sediments, Resources and Hydrocarbons*. Springer, Berlin. 1035 pp.
- Weaver, C.E., 1989. *Clays, Muds, and Shales*. Elsevier, Amsterdam, Oxford, New York, Tokyo. 819 pp.
- Wilde, V., Schultka, S., 1996. Die sandige Wealden-Fazies (Bückeburg Formation, Berrias, Unterkreide) am Westrand eines Schüttungskörpers bei Osnabrück. *Neues Jahrbuch für Geologie und Paläontologie, Abhandlungen* 199, 249–268.
- Wilson, M.E.J., Lokier, S.J., 2002. Siliciclastic and volcanoclastic influences on equatorial carbonates; insights from the Neogene of Indonesia. *Sedimentology* 49, 583–601.